

OP/QTDK'CUUGUO GP V'QHUCVGNNK'G'UVTWEVWT CN
PTQRGT VKGU'XKC'TQDWUV'UVTWEVWT CN'J GCNVJ
MQPK'QTPI

Aditi Chattopadhyay, et al.

Arizona State University
Office for Research and Sponsored Projects
1711 S. Rural Rd Adm B 160
Tempe, AZ 85287-0002

23 July 2012

Final Report

CRRTQXGF'HQT'RWDNKE'TGNGCUG=F KUVTHDWKQP'KU'WP NKO K'GF 0'



AIR FORCE RESEARCH LABORATORY
Space Vehicles Directorate
3550 Aberdeen Ave SE
AIR FORCE MATERIEL COMMAND
KIRTLAND AIR FORCE BASE, NM 87117-5776

DTIC COPY NOTICE AND SIGNATURE PAGE

Using Government drawings, specifications, or other data included in this document for any purpose other than Government procurement does not in any way obligate the U.S. Government. The fact that the Government formulated or supplied the drawings, specifications, or other data does not license the holder or any other person or corporation; or convey any rights or permission to manufacture, use, or sell any patented invention that may relate to them.

This report is the result of contracted fundamental research deemed exempt from public affairs security and policy review in accordance with SAF/AQR memorandum dated 10 Dec 08 and AFRL/CA policy clarification memorandum dated 16 Jan 09. This report is available to the general public, including foreign nationals. Copies may be obtained from the Defense Technical Information Center (DTIC) (<http://www.dtic.mil>).

AFRL-RV-PS-TR-2012-0071 HAS BEEN REVIEWED AND IS APPROVED FOR
PUBLICATION IN ACCORDANCE WITH ASSIGNED DISTRIBUTION STATEMENT

//SIGNED//
DEREK DOYLE
Program Manager

//SIGNED//
BRETT J. DEBLONK, Ph.D.
Technical Advisor, Spacecraft Component Technology Branch

//SIGNED//
B. SINGARAJU, Ph.D.
Deputy Chief, Spacecraft Technology Division
Space Vehicles Directorate

This report is published in the interest of scientific and technical information exchange, and its publication does not constitute the Government's approval or disapproval of its ideas or findings.

REPORT DOCUMENTATION PAGE				Form Approved OMB No. 0704-0188	
Public reporting burden for this collection of information is estimated to average 1 hour per response, including the time for reviewing instructions, searching existing data sources, gathering and maintaining the data needed, and completing and reviewing this collection of information. Send comments regarding this burden estimate or any other aspect of this collection of information, including suggestions for reducing this burden to Department of Defense, Washington Headquarters Services, Directorate for Information Operations and Reports (0704-0188), 1215 Jefferson Davis Highway, Suite 1204, Arlington, VA 22202-4302. Respondents should be aware that notwithstanding any other provision of law, no person shall be subject to any penalty for failing to comply with a collection of information if it does not display a currently valid OMB control number. PLEASE DO NOT RETURN YOUR FORM TO THE ABOVE ADDRESS.					
1. REPORT DATE (DD-MM-YY) 23-07-2012		2. REPORT TYPE Final Report		3. DATES COVERED (From - To) 3 Feb 2009 – 11 May 2012	
4. TITLE AND SUBTITLE On-Orbit Assessment of Satellite Structural Properties via Robust Structural Health Monitoring				5a. CONTRACT NUMBER FA9453-09-1-0316	
				5b. GRANT NUMBER	
				5c. PROGRAM ELEMENT NUMBER 62601F	
6. AUTHOR(S) Aditi Chattopadhyay, Yingtao Liu, Anthony Vizzini				5d. PROJECT NUMBER 8809	
				5e. TASK NUMBER PPM00004815	
				5f. WORK UNIT NUMBER EF003000	
7. PERFORMING ORGANIZATION NAME(S) AND ADDRESS(ES) Arizona State University Office for Research and Sponsored Projects 1711 SORural Rd Adm B 160 Tempe, AZ 85287-0002				8. PERFORMING ORGANIZATION REPORT NUMBER	
9. SPONSORING / MONITORING AGENCY NAME(S) AND ADDRESS(ES) Air Force Research Laboratory Space Vehicles Directorate 3550 Aberdeen Ave., SE Kirtland AFB, NM 87117-5776				10. SPONSOR/MONITOR'S ACRONYM(S) AFRL/RVSV	
				11. SPONSOR/MONITOR'S REPORT NUMBER(S) AFRL-RV-PS-TR-2012-0071	
12. DISTRIBUTION / AVAILABILITY STATEMENT Approved for public release; distribution is unlimited.					
13. SUPPLEMENTARY NOTES					
14. ABSTRACT This project addressed the development of an integrated Structural Health Monitoring (SHM) system for damage diagnosis, including detection and localization in complex composite structures. Lamb wave based active sensing for damage diagnosis is investigated first. The propagation of Lamb wave in stiffened carbon fiber polymer matrix composite panels is characterized. A two step damage detection and characterization approach, which uses both pulse-echo and pitch-catch active sensing schemes, is presented for the identification of delaminations in the stiffened composite panels. The Matching Pursuit Decomposition (MPD) algorithm is used for the representation of the sensor signals in the time-frequency domain. The delaminations are detected by identifying the converted Lamb wave modes in the time-frequency domain. The MPD algorithm is further used to assess the delamination location in composite structures. Due to the redundancy of the PZT sensor array, a probabilistic location estimation algorithm is used to estimate the confidence range of the delamination in the composite structures.					
15. SUBJECT TERMS SHM, MPD, damage diagnosis, localization, Lamb wave, probability					
16. SECURITY CLASSIFICATION OF:			17. LIMITATION OF ABSTRACT Unlimited	18. NUMBER OF PAGES 64	19a. NAME OF RESPONSIBLE PERSON Derek Doyle
a. REPORT Unclassified	b. ABSTRACT Unclassified	c. THIS PAGE Unclassified			19b. TELEPHONE NUMBER (include area code)

(This page intentionally left blank)

TABLE OF CONTENTS

Section	Page
1.0 SUMMARY.....	1
2.0 INTRODUCTION	2
3.0 TASK 1 REPORTING.....	5
3.1 Method, Assumptions, and Procedures.....	5
3.1.1 Composite Volume Fraction Determination.....	5
3.1.2 Mesoscale Analysis.....	9
3.1.3 Macroscale Analysis	9
3.2 Results and Discussion	10
3.2.1 Laminate Analysis	10
3.2.2 Structural Scale Analysis	11
3.2.3 Localization Analysis for Fiber and Matrix.....	13
3.2.4 Wrapping Analysis.....	14
3.3 Conclusions.....	16
4.0 TASK 2 REPORTING.....	17
4.1 Method, Assumptions, and Procedures.....	17
4.1.1 Damage Identification Procedure	17
4.1.2 Frequency Response Method of System Identification	18
4.1.3 Transfer Function Estimation Using ARX Model.....	18
4.1.4 Damage State Identification Using Damage Index.....	20
4.1.5 Experimental Setup.....	21
4.2 Results and Discussion	25
4.2.1 Frequency Response Method of Input-output MFC Transducers.....	25
4.2.2 Transfer Function Estimation and Order Selection of ARX Model	26
4.2.3 Damage Identification Using Damage Index.....	28
4.3 Conclusions.....	29
5.0 TASK 3 REPORTING.....	30
5.1 Method, Assumptions, And Procedures.....	30
5.1.1 Time-Frequency Representation of Lamb Wave using MPD.....	30
5.1.2 Experimental Setup.....	32
5.2 Results and Discussion	34

5.2.1 Group Velocity Calculation	34
5.2.2 Lamb Wave Attenuation	35
5.2.3 Global Damage Detection using Pulse-Echo Scheme	37
5.2.4 Local Damage Detection using Pitch-Catch Scheme	41
5.2.5 Damage Localization Using Time-Frequency Analysis	43
5.3 Conclusions.....	46
6.0 PROJECT CONCLUSIONS.....	48
REFERENCES	49
APPENDIX - Publications and Presentations	52

LIST OF FIGURES

Figure	Page
Figure 1. Post-Burning Samples, Burn Test 1	7
Figure 2. Post-Burning Sample, Burn Test 3	7
Figure 3. Post-Burning Sample, Burn Test 4	7
Figure 4. Pre and Post Processing of Microscope Image	8
Figure 5. Example of RUC used for mesoscale analysis	9
Figure 6. Example of RUC used for mesoscale analysis	10
Figure 7. First three natural modes from finite element analysis	12
Figure 8. Stress distribution for each ply at peak displacement	12
Figure 9. Stress distribution for each ply at peak displacement	14
Figure 10 Details of Step 8: The Wrapping Progress	15
Figure 11 Axial Stress Distribution during Wrapping Stage for All Plies	16
Figure 12. SHM of composite booms based on system identification approach	017
Figure 13. The composite boom specimen	22
Figure 14. The composite boom wrapping machine	22
Figure 15. Three damage stages for the composite boom flattening/wrapping test.	22
Figure 16. Experimental setup of vibration modal analysis	23
Figure 17. The resonant mode shift	24
Figure 18. Excitation/sensor signals and their power spectral density plots for MFC1a) and MFC4 b)	24
Figure 19. The power spectral density of input and output MFC1 and MFC4 signals at different damage states	25
Figure 20. The frequency response of input/output signal measured from MFC1 and 4 ..	26
Figure 21. Estimation error with different order number	27
Figure 22. Comparison of simulated signal and experimental signal (zoomed)	27
Figure 23. The global damage estimation	28
Figure 24. The local damage estimation between MFC1 and 2	29
Figure 25. Stiffened composite panel with bonded PZT patches	33
Figure 26. Dimensions of the composite panel and PZT patches	33
Figure 27. Flash thermography image of composite stiffened panel with 30×30mm ² delamination	33
Figure 28. (a) Signal of the Lamb wave recorded from PZT 12; (b) TFR of the Lamb wave recorded from PZT 12	34
Figure 29. Angular dependence of wave propagating velocity (S ₀ mode) in the composite panel	35
Figure 30. Wave attenuation of the S ₀ mode from PZT 12 and PZT 21	36
Figure 31. Wave attenuation of the S ₀ mode from PZT 13 and PZT 31	36
Figure 32. Normalized PZT sensor signal energy	37

Figure 33. (a) Lamb wave mode scattering into T-section; (b) Lamb wave mode scattering out of T section; (c) The different paths of Lamb wave propagation in the stiffened composite panel using the pulse-echo approach.....	38
Figure 34. Mode conversion in T section	39
Figure 35. TFR and mode identification of the echo Lamb wave in the healthy stiffened panel.....	41
Figure 36. TFR and mode identification of the echo Lamb wave using the stiffened panel with delamination	41
Figure 37. Possible propagation paths for PZT 21	42
Figure 38. TFR of Lamb wave collected from PZT 21 using a healthy panel	42
Figure 39. TFR of Lamb wave collected from PZT 31 using a healthy composite panel	43
Figure 40. TFR of Lamb wave collected from PZT31 using composite panel with delaminations.....	43
Figure 41. Composite plates and stiffened panels used in experiments	44
Figure 42. TFRs of the Lamb wave signals collected from master sensor in healthy plate, master and slave sensors from damaged plate.....	45
Figure 43. Estimated delamination position and confidence range: a) quasi-isotropic composite panels; b) orthotropic composite panels; c) composite panels with two stiffeners.	46

LIST OF TABLES

Table	Page
Table 1. Resin Burn Off Test Results	7
Table 2. Mesoscale Elastic Properties	9
Table 3. Macroscale Weave Ply Elastic Properties	10
Table 4. Macroscale Weave Ply Elastic Properties	10
Table 5. Mesoscale Elastic Properties	11
Table 6. The First Five Resonant Mode of Boom Structure.....	11
Table 7. The ToF analysis for the S_0 mode	38
Table 8. The ToF analysis for the A_0 mode.....	39
Table 9. The ToF comparison for the S_0 modes	40
Table 10. The real and estimated delamination positions.....	46

EXECUTIVE SUMMARY

This project addressed the development of an integrated Structural Health Monitoring (SHM) system for damage diagnosis, including detection and localization, in complex composite structures. Lamb wave based active sensing for damage diagnosis is investigated for both 1-D and 2-D specimens. The propagation of Lamb waves in stiffened carbon fiber polymer matrix composite parts is characterized. A damage detection and characterization approach, which uses both pulse-echo and pitch-catch active sensing schemes, is presented for the identification of delaminations in the stiffened composite parts. The Matching Pursuit Decomposition (MPD) algorithm is developed and used for the representation of the sensor signals in the time-frequency domain. The delaminations are detected by identifying the converted Lamb wave modes in the time-frequency domain. The MPD algorithm is further used to assess the delamination location in composite structures. A process is described that allows damage localization without insight into the composite layup and the anisotropic nature of wave group velocities is accounted for by the sensing strategy and through data processing.

1.0 SUMMARY

This project addressed the development of an integrated Structural Health Monitoring (SHM) system for damage diagnosis, including detection and localization, in complex composite structures for use by future DOD platforms. Lamb wave based active sensing for damage diagnosis is investigated first. The propagation of Lamb wave in stiffened carbon fiber polymer matrix composite beams and panels is characterized. A damage detection and characterization approach, which uses both pulse-echo and pitch-catch active sensing schemes, is presented for the identification of delaminations in the stiffened composite parts. The Matching Pursuit Decomposition (MPD) algorithm is developed and used for the representation of the sensor signals in the time-frequency domain. Composite degradation is detected by identifying the converted Lamb wave modes in the time-frequency domain. The MPD algorithm is further used to assess the delamination location in rib-stiffened composite panels. The sensor locations and differences in Time-of-Flight (ToF) are used to formulate three nonlinear equations. The nonlinear equations are converted into an unconstrained optimization problem and solved using Newton's method. Due to the redundancy of the PZT sensor array, a probabilistic location estimation algorithm is used to estimate the confidence range of the delamination in the composite panels. This research can be characterized by the following efforts:

Task 1: Multiscale Analysis of Composite Structures

- Determine method for defining material properties of a given layup
- Perform Multiscale analysis with defined material properties
- Apply technique to relevant 1-D specimen

Task 2: Development of Signal Processing Techniques for SHM

- Time Domain
- Frequency Domain
- Apply technique to relevant 1-D specimen

Task 3: Final Application of developed techniques to a Complex Specimen

- Refine preferred signal processing for 2-D propagation
- Global analysis
- Local analysis

2.0 INTRODUCTION

Interest in SHM techniques and Damage Prognosis (DP) has increased significantly over the last few years. Well-developed DP and SHM systems inform the users about the presence of incipient damage and provide estimation of the Remaining Useful Life (RUL) of the structures [1-3]. The ultimate goal is to shift from schedule-based inspection to Condition-Based Maintenance (CBM), which can cut down the maintenance time, and reduce cost and labor requirements. Most importantly, successful implementation of these methodologies will increase the confidence levels in operating the systems and improve user safety. There is a growing interest in the utility of SHM for space systems. The sensing methodology could be implemented on satellite components during the Assembly, Integration, and Test (AI&T) phase or while on-orbit to track damage and provide real-time information.

Although composite materials have been widely used as primary structural components in many industries, such as aerospace, automotive and marine, the characterization, detection and quantification of multiscale damage in these heterogeneous material systems remain critical areas of research. Significant research efforts have been devoted to the solution of these problems in the last decade. Among various technologies under investigation, one of the most popular approaches for damage detection in composites is Guided Wave (GW) based SHM techniques. These techniques involve exciting the structures with high frequency elastic waves and processing the different sensing response to detect and characterize damage within structures. When stress waves are forced to follow a path by the material boundaries, such as for thin plates and beams, the GW is usually specified as a Lamb wave. Since aerospace and ground vehicles are fundamentally composed of simple beam, plate and shell structures, Lamb wave based techniques are applicable in developing SHM framework for such systems. More details into the propagation of the Lamb waves can be found in [6-10]. Surface-bonded/embedded piezoelectric wafer transducers are widely used as sensors and actuators [4-5] in aerospace applications. Compared to traditional SHM approaches using strain gages or Fiber Bragg Grating (FBG) sensors, the advantage of Lamb wave is that an actuator-sensor pair has a large coverage area so that the density of sensors and actuators can be low. This advantage allows the Lamb wave based SHM techniques to be used for monitoring large scale structures.

Most previous research using Lamb wave based damage detection approaches focused on simple composite structures, such as plates and beams. Fasel et al. used ultrasonic chaotic excitations to detect various damage conditions of composite bonded joint [11]. A statistical classification algorithm was used to correlate the real damage state. Lu et al. studied the mechanism of Lamb wave propagation in a stiffened panel in the time domain [12]. Correlation analysis techniques were used for the damage identification and location. Banerjee et al. used low frequency modal vibrations to detect impact damage and used high frequency passive Lamb wave sensing modes to localize the damage [13]. Lamb wave sensing signals are also complex in nature. More than one mode can be generated in a Lamb wave at any excitation frequency and each mode has a unique dispersion curve. Most the aforementioned work did not study Lamb wave propagation characteristics in stiffened composite panels with complex

geometries. The mechanism of mode decomposition and mode conversion due to geometric discontinuities and material imperfection is still not fully understood. It is important to develop efficient analysis techniques to study the Lamb wave signals, isolate different Lamb wave modes, and extract useful information for damage detection, identification, localization, and RUL estimations in composite structures.

Damage localization in composite structures requires accurate GW information and features. Most previous work focused on locating impact damage in composite structures using passive sensing approaches [14-16]. A traditional damage localization technique is to use the triangulation method and the ToF information to obtain three ellipses requiring at least three active sensors. The intersection point of the three ellipses is considered to be the damage spot. Knowledge of the group velocities of the guided wave in all directions is required for this approach [17, 18]. Neural network algorithms have been used to obtain the angle dependent group velocity profile [19]. Other damage localization approaches include direct wave path analysis between an actuator and multiple sensors [8], the energy decay model [20], principle stress directions for impact locations [21], use of Laser Doppler Vibrometer (LDV) [22] and FBG sensors [16, 23]. These approaches have been validated using isotropic and quasi-isotropic plates with simple geometries. However, only a limited amount of work has addressed the extension of damage localization to general anisotropic composite structures with complex geometries.

Signal processing is necessary for extracting features for damage detection and localization in composite structures. The goal of signal processing is to not only extract information from the sensing signal for damage detection, but also to provide useful features for the damage characterization and quantification, which is important for damage state awareness and prognosis. The traditional Fourier transform method provides the ‘global’ information about the frequency and is suitable for signals with stationary frequency content. However, the frequency content of a Lamb wave signal varies in the time domain. This type of signal can be better represented in the time-frequency domain to extract time-varying frequency information. To analyze the time-varying sensor response effectively, the time and frequency domain characteristics must be considered simultaneously. These Time-Frequency Representations (TFRs) characterize a given signal over the time-frequency plane by combining the time and frequency domain data. This yields more revealing information about the temporal localization of a signal’s spectral components. The Matching Pursuit Decomposition (MPD) is a time-frequency based technique that decomposes a signal into highly localized time-frequency atoms and can provide a highly concentrated TFR [24]. It is an iterative algorithm that decomposes any signal into a linear expansion of waveforms that belong to a redundant dictionary. The MPD dictionary consists of a collection of time-frequency atoms that are the dilated (time-scaled), translated (time-shifted) and modulated (frequency-shifted) versions of a single basic atom. The basic atom is often chosen to be a Gaussian signal because Gaussian signals are the most concentrated signals in both time and frequency. The MPD method has been applied in damage detection of both metallic and composite structures. Das et al. [25] developed a Monte Carlo MPD method for damage quantification in simple composite structures. But the developed algorithm was only validated by detecting and localizing damages in 12-

inch long composite beams. Chakraborty et al. [26] used a MPD algorithm to classify the fastener failure damage in aluminum plates. The extension of MPD method to the damage detection and feature extraction of complex composite structures has not been fully explored.

To clearly explain the work done in each task, each of the four efforts will be discussed separately with methods, results and conclusions addressed solely for the specific effort prior to continuing on to subsequent tasks.

3.0 TASK 1 REPORTING

In order to adequately model composite structures, a multi-scale analysis approach is required to capture the interaction of the various plies and resin matrix. This section of the report will detail the work completed in modeling multi-layered composites and is applied to a complex beam specimen provided by the program manager.

3.1 Method, Assumptions, and Procedures

3.1.1 Composite Volume Fraction Determination

To model a composite, steps must be taken to characterize a layup and the material used to build the structure. Multiple test methods are known for determining fiber volume fraction in fiber-reinforced composites. Photomicrography can be used to determine the fiber volume fraction of a cross-sectional area of the specimen, which is used to estimate the overall specimen fiber volume fraction. Chemical digestion is a destructive method used, described in ASTM D3171, this technique involves using an acid to remove resin from the sample while leaving the fibers unaffected.

The program manager provided composite beams from AFRL/RVSV, known as TRAC booms. The boom structures are comprised of two constituents, the IM-7 fiber and 977-2 epoxy matrix. The boom specimen in this study is composed of two flanges and each flange has six plies. The top two plies and bottom two plies use unidirectional carbon fiber tape and the middle two plies use $\pm 45^\circ$ plain weave fiber fabric.

A resin burn-off technique was used in this case for determining the fiber volume fraction of the TRAC boom specimen. Resin burn-off is a technique which is used to burn the resin from the test specimen, while leaving the only the fibers from the specimen remaining. With a known density of both resin and fiber, the fiber volume fraction can be determined by measuring the mass of the specimen before and after resin burn-off. ASTM D2584-02 is the testing standard for determining the ignition loss of cured reinforced resins.

The standard ASTM D2584-02 was followed for the first burn-off test conducted, however a few changes were necessary based on material availability. Three samples were used for each test, each approximately 1" in length. Each specimen was assigned an individual aluminum foil crucible, with dimensions of 3" in diameter, 1/2" in depth. The mass of each specimen's assigned crucible was measured while using a Sartorius BP 110S analytical balance, featuring readability of 0.0001g. The mass of each healthy sample-in-crucible mass was then measured prior to burning. Burning was conducted in a Fisher Isotemp 550 Muffle Furnace.

Multiple burning specifications were necessary to properly burn off the resin of the specimens. Initially, the ASTM standard's temperature specification was followed, calling for specimen burning at 565°C for a time of up to 6 hours. The upper time limit of 6 hours was used in the first burning test. Crucible mass during burning was found to remain unchanged, found by the burning of an empty crucible and measuring mass change. It should be noted that specimens were placed inside the muffle furnace for the

entire heat-up period, which was approximately 15 minutes for the temperature range used in testing. The resulting specimens after burn-off test 1 are shown in Figure 1. The resin was fully removed from the specimen using the first burning specifications; however the fibers themselves were completely destroyed, leaving only ash in each of the 3 sample crucibles. Burn-off mass was calculated to be near 99% for each of the 3 specimens, concluding that this burning procedure was too hot for the fibers.

A second burn was conducted following the same procedure as the first burn; however burning conditions were changed with focus on allowing survival of the fibers during burning. The second burn test was conducted at 370°C for 2 hours. Burn results clearly revealed the resin was not fully cooked off, as the samples still retained a much higher level of stiffness than would be found if resin was not present. A third test was performed at 425°C for 3 hours, yielding samples as shown in Figure 2. These samples clearly showed a greater level of resin burn-off than test 2. Resin was still present, however the fibers remained healthy. A volume fraction of 75% was calculated during this test, suggesting the cooking procedure did not quite allow complete burn-off of the specimen resin.

The ideal burning specification was found from the result of test 4, which was cooked at 475°C for 3 hours. This test resulted in complete resin burn-off, leaving the fibers in an undamaged state. The post-burning samples yielded no resemblance to the original specimen, but instead yielded the form of a pile of carbon fiber sheets with hair-like consistency. The resulting post-burn sample is shown in Figure 3.

The volume fraction was calculated using Equation 1, where ρ_m is the resin density, ρ_f is the fiber density, W_f is the fiber weight, and W_m is the matrix weight.

$$V_f = \frac{\rho_m W_f}{\rho_f W_m + \rho_m W_f} \quad 1)$$

The density of the fiber was found from the manufacturer specification, with a value of 1.78kg/m³. Resin density was found from the manufacturer specifications, with a value specified of 1.31kg/ m³. The resulting fiber volume fraction was found for each specimen cooked using the test 4 burning specification, and results are shown in Table 1. The average fiber volume fraction for the test set was found to equal 57.6%. A range calculation was performed on the experimental results, with up to a 10% variation of both fiber and resin density used. The perturbed results yielded a range of 52.6% to 62.4% fiber volume fraction for the specified range of densities, which used the experimental average as the base point. The experimental results using the density variations yielded results close to that of the photomicrography testing, which determined the fiber volume fraction to be approximately 50%.



Figure 1. Post-Burning Samples, Burn Test 1



Figure 2. Post-Burning Sample, Burn Test 3



Figure 3. Post-Burning Sample, Burn Test 4

Table 1. Resin Burn Off Test Results

Sample	Crucible Mass(g)	Healthy Sample, in Crucible Mass(g)	Cooked Sample, in Crucible Mass(g)	Experimental Fiber Volume Fraction
1	2.2838	4.4296	3.6400	0.558
2	2.3291	4.2290	3.5735	0.583
3	2.2540	4.3270	3.6033	0.578
4	2.2651	4.2927	3.5735	0.572
5	2.2710	4.3285	3.6033	0.575
6	2.2658	4.2147	3.5488	0.586
7	2.2563	4.2287	3.5428	0.580
8	2.2702	4.1747	3.5018	0.574
9	2.2561	4.3187	3.5916	0.575
			Average	0.576
			Standard Deviation	0.008

Since each flange of the boom laminate costs of 10 plies and 2 of those plies are fabric laminate, it is not safe to assume that the previously determined volume fraction can be applied to each ply. However the following assumptions can be made:

- Unidirectional (tape) plies have equivalent volume fractions
- Fabric plies have equivalent volume fractions
- Tows within the fabric plies have the same volume fraction as the tape plies

It is difficult to determine the ply level volume fraction of the fabric plies. The previous work used optical microscopy to determine the ply level microstructure. The volume fractions at each and the tow were determined by counting the number of fibers in an image and dividing over the area. These results conflicted with the global volume fraction measurements due to the inaccuracy of the manual calculations. The microscopy images were post processed such that the fiber area is clearly represented

in an image and the volume fraction could be measured through OOF2 software from NIST. The different images are shown in Figure 4. The corrected volume fractions were determined to be approximately 61%.

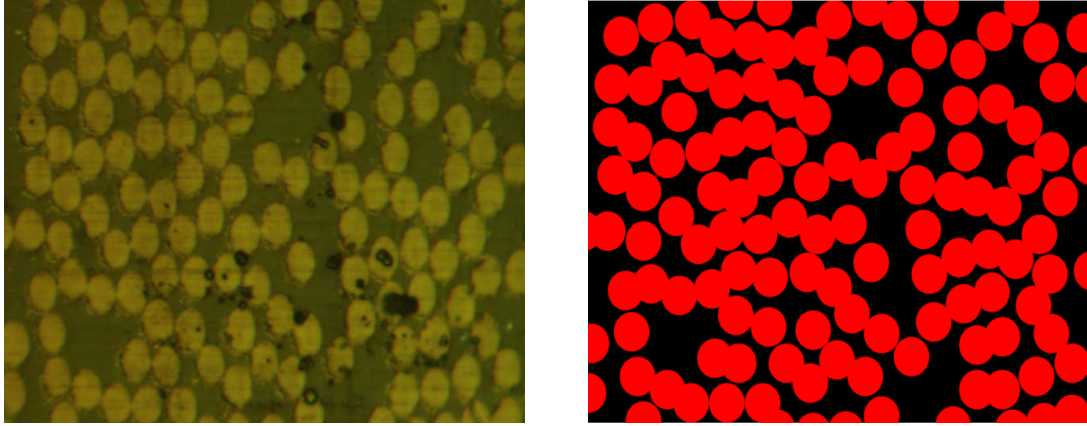


Figure 4. Pre and Post Processing of Microscope Image

The global volume fraction can be related to each individual ply volume fraction from the following relationship, where t is the thickness and n denotes ply level properties.

$$V_f = \frac{1}{t} \sum_{n=1}^p V_f^n t^n \quad 2)$$

This equation can then be expanded to the following form for the particular case of the boom laminate:

$$V_f = \frac{1}{t} \left[\frac{2}{3} t V_f^{tape} + \frac{1}{3} t V_f^{fabric} \right] \quad 3)$$

This allows the fabric ply volume fraction to be expressed in terms of the known quantities of the tape and global volume fractions, as shown below:

$$V_f^{fabric} = 3V_f - 2V_f^{tape} \quad 4)$$

Using the resin burn off results and the microscopy characterization, the fabric volume fraction was determined to be 49%. To complete the multiscale analysis the cross sectional area of the fabric tows needed to be calculated in order to approach a close approximation of the microstructure of the fabric.

3.1.2 Mesoscale Analysis

At the mesoscale a refined RUC was used to analyze the fiber/matrix RUC in the tows and the tape plies. The RUC had to be reanalyzed from the previous quarter in light of the new mesoscale volume fraction. Previously, a 2x2 RUC was used to model the fiber/matrix, a new RUC was designed with a 19x19 grid. This is shown below the updated mesoscale elastic properties are shown in Table 2. Mesoscale Elastic Properties

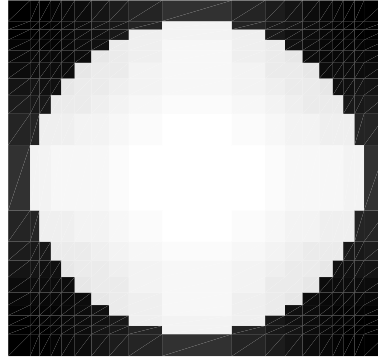


Figure 5. Example of RUC used for mesoscale analysis

Table 2. Mesoscale Elastic Properties

E_A	E_T	ν_A	ν_T	G_T
169 GPa	6.76 GPa	0.31	0.27	3.78 GPa

3.1.3 Macroscale Analysis

The RUC for the plain weave plies was reanalyzed with the new volume fraction as well as using the new 19x19 RUC. The dimensioned plain weave is shown in Figure 6 and the new dimensions of the plain weave RUC are shown in table below.

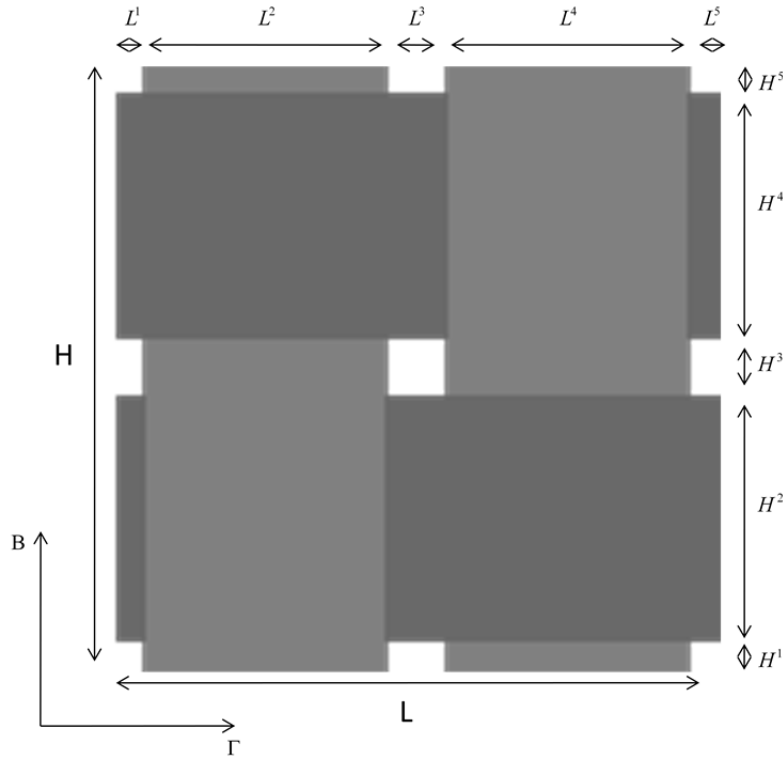


Figure 6. Example of RUC used for mesoscale analysis

Table 3. Macroscale Weave Ply Elastic Properties

Parameter	Magnitude (mm)
H^1, H^5, L^1, L^5	0.275mm
H^2, H^4, L^2, L^4	2.25mm
H^3, L^3	0.55mm
H, L	5.6mm

Table 4. Macroscale Weave Ply Elastic Properties

E_A	E_T	ν_A	ν_T	G_T
52 GPa	52 GPa	0.04	0.04	2.21 GPa

3.2 Results and Discussion

3.2.1 Laminate Analysis

For the guided wave analysis, the laminate elastic properties had to be determined. This was accomplished through use of classical lamination theory in conjunction with the macroscale and mesoscale results. The ABD matrix was determined as well as the engineering elastic constants for the laminate. It is important to note here that the in

plane Poisson's ratio is predicted to be greater than 0.5. This makes the laminate material difficult to apply to elasticity solutions.

$$ABD = \begin{bmatrix} 123.16 & 9.65 & 0 & 0 & 0 & 0 \\ 9.65 & 14.42 & 0 & 0 & 0 & 0 \\ 0 & 0 & 10.98 & 0 & 0 & 0 \\ 0 & 0 & 0 & 13.73 & 0.23 & 0 \\ 0 & 0 & 0 & 0.23 & 0.64 & 0 \\ 0 & 0 & 0 & 0 & 0 & 0.38 \end{bmatrix} \text{ kN/m} \quad 5)$$

Table 5. Mesoscale Elastic Properties

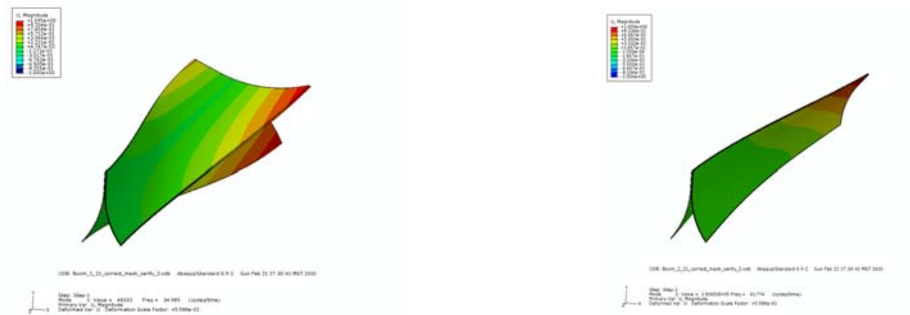
E ₁	E ₂	v ₁₂	G ₁₂
117 GPa	13.7 GPa	0.67	10.9 GPa

3.2.2 Structural Scale Analysis

The Abaqus simulation of both the modal frequencies and damage induction procedure were rerun with corrected material properties. The corrected modal frequencies are stress distributions are shown below. A detailed study on mesh convergence was also performed to check requirements for element size and type. Final result yielded elements of approximately 2mm characteristic length for quadratic elements.

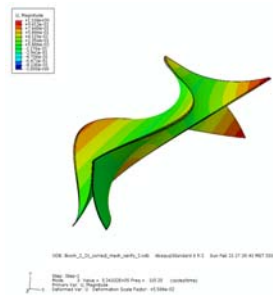
Table 6. The First Five Resonant Mode of Boom Structure

Mode 1 (Hz)	Mode 2 (Hz)	Mode 3 (Hz)	Mode 4 (Hz)	Mode 5 (Hz)
54.97	70.40	151.45	192.14	219.88



Mode 1. Frequency: 34.98 Hz

(b) Mode 2. Frequency: 61.77 Hz



(c) Mode 3. Frequency: 115.25 Hz

Figure 7. First three natural modes from finite element analysis

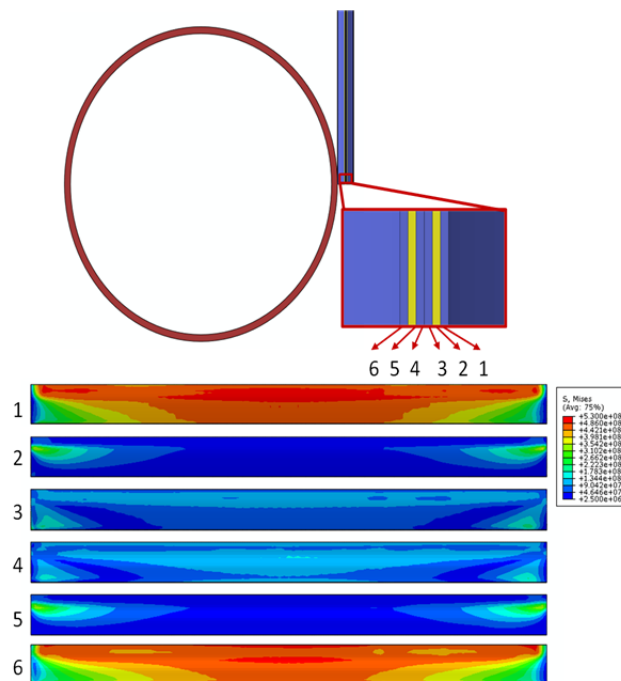


Figure 8. Stress distribution for each ply at peak displacement

3.2.3 Localization Analysis for Fiber and Matrix

Extensive localization was investigated to determine hot spots and key areas of interest for microcracking and structural degradation. Localization was determined by using the strain output at the centroids of the highest strain regions in the finite element analysis as boundary conditions for the macro-micro model. The localization was carried at as a ply level analysis and the stresses down to the microscale were determined. Previous the macroscale relationship was given by:

$$\sigma^{macro} = C^{macro} \epsilon^{macro} \quad (6)$$

Using the strains from the finite element analysis results the stress can be rewritten as:

$$\sigma^{macro} = C^{macro} \epsilon^{FEM} \quad (7)$$

The stiffness is also known in terms of the macroscale geometric properties and concentration matrices and can be substituted into 7), which yields the following.

$$\sigma^{macro} = \frac{1}{HL} \sum_B^{n_B} \sum_\Gamma^{n_\Gamma} C^{B\Gamma} A^{B\Gamma} H^B L^\Gamma \epsilon^{FEM} \quad (8)$$

where H and L are height and length of the RUC as shown in Figure 6 and A is concentration matrix and C is the stiffness. To localize the results from the finite element analysis, the localized strains can be applied through the double homogenization process and the micro stresses can be written in terms of finite element analysis strain. The final

$$\sigma^{micro} = C^{micro} A^{micro-meso} A^{meso-macro} \epsilon^{fem} \quad (9)$$

A tree level plot showing the localization of stresses is shown below.

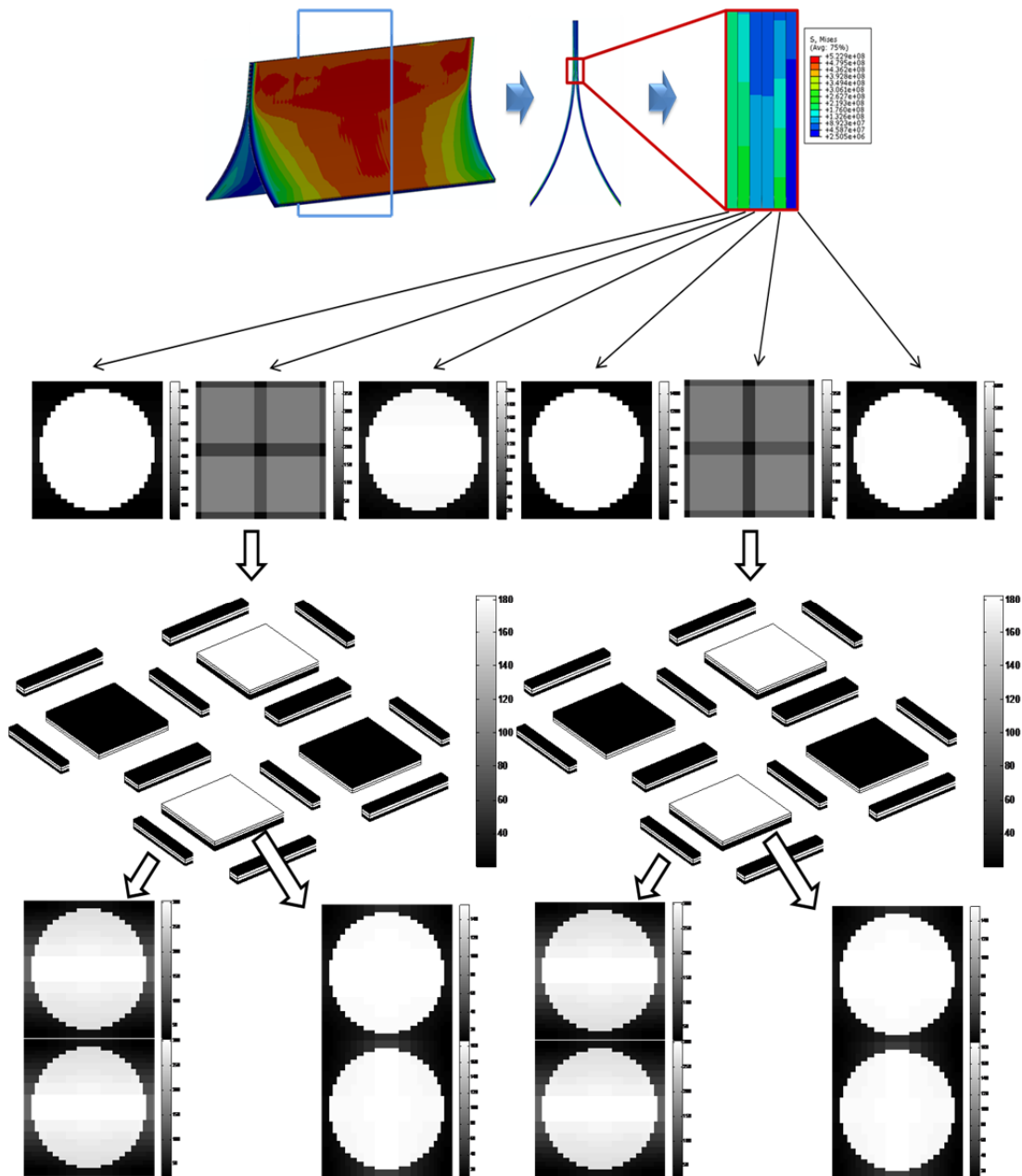


Figure 9. Stress distribution for each ply at peak displacement

3.2.4 Wrapping Analysis

As with the previous modal analysis, the numerical simulation of the wrapping induced damage is necessary as a corollary to the experimental portion. This model will be used to induce damage in the boom such that a modal analysis can be performed for a damaged state. The FE model consists of three main components: the hub, roller, and boom. The complete analysis consists of 8 steps, but they are grouped into 4 important category: compress one flange end of boom, gradually compress the

area near the edge, contact boom to roller, rotate roller. The clamp was not necessary in the model because the boundary condition was applied through displacement control. The final step rotates the hub so that the boom wraps around. The most important boundary conditions are in the final step. The process and resulting stress are seen below. For the booms in this study, most damage is assumed to be induced during the wrapping process, which occurs in the final step of the stow process. A detailed breakdown of the eight step model is shown in Figure 10. In the FE model, the same layup structure that was used in the modal analysis , Figure 9, was employed. In the analysis there are a total of 6 plies representing 10 plies. At the final state the linear stresses for each ply can be seen from Figure 11. In those figures, ply number 1 represents the outermost ply when wrapping and ply number 6 represents the innermost ply. An important observation to be made is that the stress distributions are far from symmetric about the ply 3-4 interface. The damage is mostly contained to the bonded regions of the flanges. The weave plies show little to no damage by the Tsai Hill failure criteria, an advanced theory may be necessary to capture these effects.

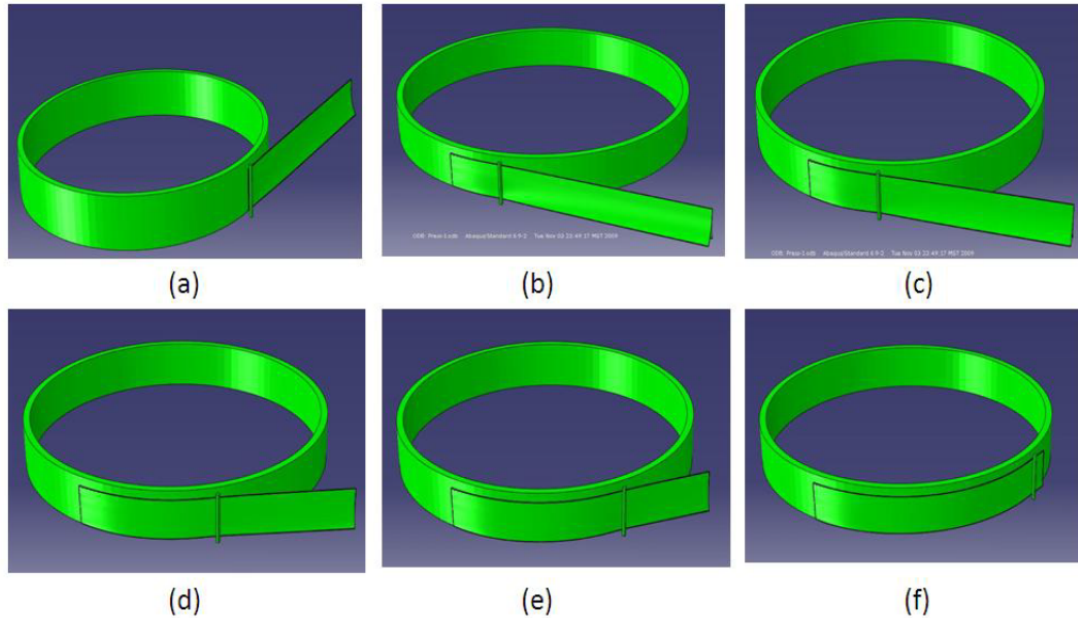


Figure 10 Details of Step 8: The Wrapping Progress

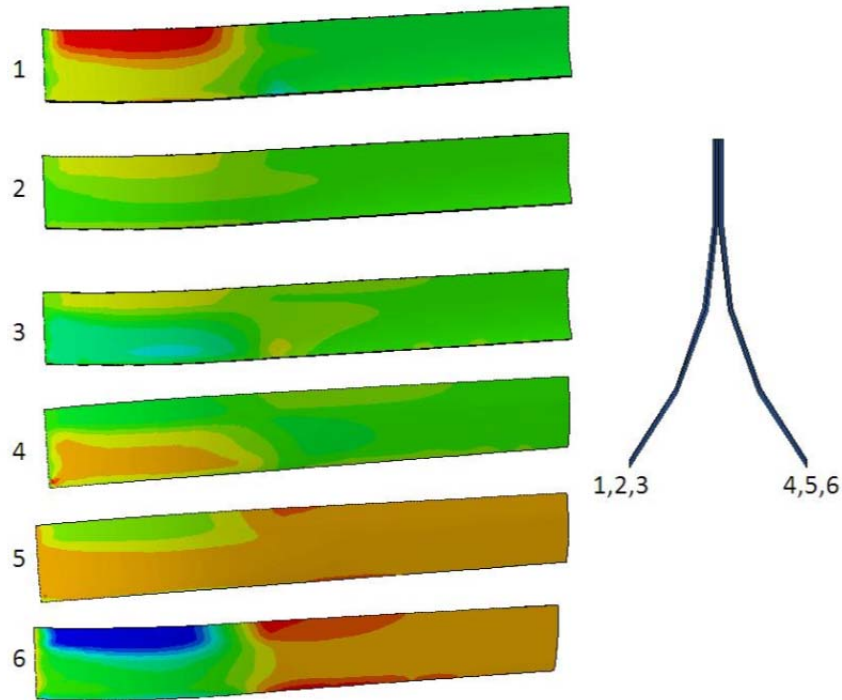


Figure 11 Axial Stress Distribution during Wrapping Stage for All Plies

3.3 Conclusions

This effort focused on developing the steps needed to characterize a composite laminate and develop the multi-scale elements required to accurately model a composite laminate structure. The process was applied to AFRL/RVSV TRAC booms provided by the program manager and demonstrated that by accurately representing the multi-scale elements of a given structure, a reasonable estimate of the stresses in the composite under deformation can be tracked. Modeling shows that the majority of the damage occurs at the joint where both flanges meet and the wrapping process causes more microcracking than flattening the flanged sections. The following task will now go into the experimental work done with SHM and signal processing which can then be used to compare with results from this task.

4.0 TASK 2 REPORTING

Matrix cracks are considered to be the primary form of damage caused by flattening and wrapping TRAC boom around the mounting hub. A well-developed Structural Health Monitoring (SHM) system tasked with monitoring structural degradation will provide information for the dynamic control of the satellite and the condition of deployable mechanisms on the space vehicle. In this section, a novel SHM methodology based on system identification techniques is presented to identify the damage in laminated composite booms. Non-Destructive Evaluation (NDE) techniques, frequency response analysis and Auto-Regressive with eXogenous (ARX) input models are used to approximate the transfer functions between input and output sensing signals. Structural degradation is identified by examining the change of transfer functions at different damage states. A single-input-single-output (SISO) approach is adopted in this section. System identification techniques allow characterizing of structural degradation without the need for acquiring excessive training data. The proposed methodology is verified through experimentation where damage is gradually induced by flattening and wrapping deployable boom samples around a circular hub.

4.1 Method, Assumptions, and Procedures

4.1.1 Damage Identification Procedure

An overview of the system identification based approach is shown in Figure 12. Using a MFC actuator, the sensor signals are recorded. Frequency response analysis is used to understand the patterns of structural transfer functions. The system model has been constructed experimentally using the ARX model. Damage states are identified by extracting features from the residual estimation errors of the ARX model. In this research, flexible MFC transducers are used as both actuator and sensors to measure the response of the composite booms at different damage states.

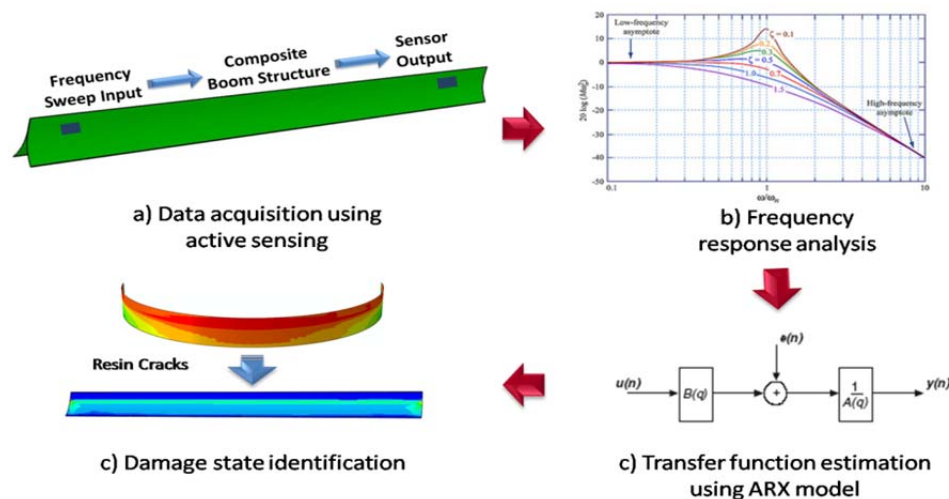


Figure 12. SHM of composite booms based on system identification approach

4.1.2 Frequency Response Method of System Identification

The frequency response method for system identification characterizes the response of the composite boom subject to sweep excitation. The frequency response is estimated using spectral analysis and can be expressed in a cross-correlation function and auto-correlation function. For time domain input signal $x(t)$ and output signal $y(t)$, the spectral densities $S_{yx}(j\omega)$ and $S_{xx}(j\omega)$ of the relevant measured input and output are written as [27]:

$$S_{yx}(j\omega) = \tilde{y}(j\omega)\tilde{x}^*(j\omega) \quad (10)$$

$$S_{xx}(j\omega) = \tilde{x}(j\omega)\tilde{x}^*(j\omega) \quad (11)$$

where output $\tilde{x}(j\omega)$ and $\tilde{y}(j\omega)$ are the finite Fourier transforms of the relevant measured input and output, and $\tilde{x}^*(j\omega)$ is the conjugate of $\tilde{x}(j\omega)$.

By applying the finite Fourier transform to measured input and output data, an estimate of the frequency response function can be written as,

$$G(j\omega) = \frac{S_{yx}(j\omega)}{S_{xx}(j\omega)} = \frac{\tilde{y}(j\omega)\tilde{x}^*(j\omega)}{\tilde{x}(j\omega)\tilde{x}^*(j\omega)} \quad (12)$$

where the frequency response function $G(j\omega)$ is a complex vector. Both input-output amplitude ratio and phase shift are considered. The amplitude ratio $R(\omega)$ and phase $\phi(\omega)$ can be expressed as,

$$R(\omega) = \sqrt{\{\text{Re}[G(j\omega)]\}^2 + \{\text{Im}[G(j\omega)]\}^2} \quad (13)$$

$$\phi(\omega) = \tan^{-1}\left\{\frac{\text{Im}[G(j\omega)]}{\text{Re}[G(j\omega)]}\right\} \quad (14)$$

The frequency response method constitutes a describing function which linearly characterizes the behavior of the input-to-output MFC transducers. Plotting $20\log_{10}R(\omega)$ and $\phi(\omega)$ versus $\log_{10}(\omega)$ results in a Bode plot, which shows the linear transfer function. Once the transfer function of MFC transducers changes due to induced damage, the Bode plot of input-output sensor measurements will indicate the change of transfer function and provide guidance for the future construction of a system transfer function model.

4.1.3 Transfer Function Estimation Using ARX Model

For composites with microscale damages, the input-output model can be reasonably estimated by the ARX model and linear least squares method. Ignoring the estimation error, ARX model which describes the relationship between input $x(t)$ and output $y(t)$, is shown in Eq. 15) [28]:

$$y(t) + a_1y(t-1) + \dots + a_ny(t-n) = b_1x(t-1) + \dots + b_mx(t-m) \quad (15)$$

The model assumes that the sampling interval is uniform in the time domain. In order to determine the next output value given by previous observation, it is easier to write Eq. 15) as:

$$y(t) = -a_1 y(t-1) - \dots - a_n y(t-n) + b_1 x(t-1) + \dots + b_m x(t-m) \quad 16)$$

The parameters of the ARX model a_i and b_j are calculated from sensor measurement $x(t), y(t)$ using linear least squares method. For more compact notation, these adjustable parameters can be written in a vector form:

$$\theta = [a_1 \dots a_n b_1 \dots b_m]^T \quad 17)$$

and the previous input-output measurement can be written as:

$$\varphi = [-y(t-1) \dots -y(t-n) x(t-1) \dots x(t-m)]^T \quad 18)$$

According to Eq. 18), the output estimation of ARX model is:

$$y(t) = \varphi^T(t)\theta \quad 19)$$

It is noted that the calculation of the next output measurement from previous data in vector φ depends on all the parameters in vector θ . The calculated value $\hat{y}(t|\theta)$ is different from the real measurement $y(t)$.

$$\hat{y}(t|\theta) = \varphi^T(t)\theta \quad 20)$$

All the unknown parameters in vector θ are calculated using the least squares method. From the recorded input-output measurement R^N , the unknown parameters can be calculated by minimizing the error, $E(\theta, R^N)$ between real output measurement $y(t)$ and calculated output $\hat{y}(t|\theta)$. Here,

$$R^N = [x(1) y(1) \dots x(N) y(N)] \quad 21)$$

$$E(\theta, R^N) = \frac{1}{N} \sum_{i=1}^N (y(t) - \hat{y}(t|\theta))^2 = \frac{1}{N} \sum_{i=1}^N (y(t) - \varphi^T(t)\theta)^2 \quad 22)$$

Set the derivative of $E(\theta, R^N)$ to zero,

$$\frac{d}{d\theta} E(\theta, R^N) = \frac{2}{N} \sum_{i=1}^N \varphi(t)(y(t) - \varphi^T(t)\theta) = 0 \quad 23)$$

resulting in,

$$\sum_{i=1}^N \varphi(t)y(t) = \sum_{i=1}^N \varphi(t)\varphi^T(t)\theta \quad (24)$$

Because $\varphi(t)$ has been defined by the previous input-output measurement, all the parameters for ARX model can be calculated using Eq. 25).

$$\theta = \left[\sum_{i=1}^N \varphi(t)\varphi^T(t) \right]^{-1} \sum_{i=1}^N \varphi(t)y(t) \quad (25)$$

The goal of system identification is to obtain the transfer function that predicts the output using input of the system reliably. From a given set of experimental data, the modeled data $\hat{y}(t|\theta)$ is compared with the experimental data $y(t)$ to minimize the error between the two data sets. Once θ is calculated, the transfer function can be obtained from Eq. 19).

4.1.4 Damage State Identification Using Damage Index

The accuracy and sensitivity of the defined damage index is critical for identifying matrix cracks in composites. Ideally, a composite structure without damage can be reasonably modeled as a linear system. However, composite structures present more nonlinear properties when non-visible damages, such as matrix cracks, are introduced [29-31]. Although the ARX model can be expressed as shown in Eq. 15), an error term should be introduced to this model for the reconstruction accuracy. The modified ARX model can be expressed as,

$$\begin{aligned} y(t) + a_1y(t-1) + \dots + a_ny(t-n) \\ = b_1x(t-1) + \dots + b_mx(t-m) + \varepsilon(t) \end{aligned} \quad (26)$$

where $\varepsilon(t)$ is the estimation error. It is assumed that the error between the measurement and estimation obtained by the ARX model is mainly caused by the nonlinear properties of damaged composites. The estimation error becomes larger when more nonlinearities due to damage are introduced. A clear definition of estimation error $\varepsilon_s(t)$ at damage state s is expressed as:

$$\varepsilon_s(t) = y_s(t) + \sum_{i=1}^n a_{i,s}y_s(t-i) - \sum_{j=1}^m b_{j,s}x_s(t-j) \quad (27)$$

where $a_{i,s}$ and $b_{j,s}$ are the parameters of ARX model at damage state s , $y_s(t-i)$ ($i = 0, 1, \dots, n$) are the sensor output measurement at damage state s , and $x_s(t-j)$ ($j = 1, 2, \dots, m$) are the sensor output measurement at damage state s . By carefully choosing the order of the ARX model, a novel damage index can be defined as:

$$DI_s = \sqrt{\frac{[\varepsilon_s(t) - \varepsilon_0(t)]^2}{\varepsilon_0^2(t)}} \quad 28)$$

where $\varepsilon_0(t)$ is the estimation error for the reference damage level. When the healthy state of the structures is known, the damage state $\varepsilon_s(t)$ is the s^{th} damage state with respect to the healthy state ($s=0$). However, when the healthy state is unknown, the defined damage index DI_s can still be used to compare the later damage state with the reference damage level (the first available damage state).

4.1.5 Experimental Setup

A supplied boom specimen was instrumented with four MFC transducers and three strain gages. The MFCs used were manufactured by Smart Material Corp. (Model: M 2814 P1). The composite boom specimen with surface mounted sensors is shown in Figure 13. In order to obtain proper bonding conditions between the boom and the sensors, the sample surface was prepared with abrasive paper and cleaned with cotton tipped applicator. Stewart-MacDonald super glue (Model 20-X) was used as the adhesive. The primary source of damage to the boom structure is the flattening and wrapping process of the boom around a hub that is used to transport the boom prior to deployment. The extent of damage due to wrapping the boom around the hub is critical in the system response, as the stiffness change due to matrix microcracking will affect the system's response. The damage incurred by the real boom structures has been simulated experimentally using a wrapping fixture, as shown in Figure 14. The wrapping fixture consists of a 14" diameter hub around which the boom sample is wound. This fixture was constructed to test 24" samples. The boom was clamped as shown in Figure 14 with a 2 inch long clamping surface, flattening the clamped end of the boom to the hub. The boom was then wrapped taut around the center hub and clamped at the preset location for 30 seconds. The rate of wrapping was approximately 1 inch per second, which was necessary to ensure the boom flattened properly and maintain as little gap as possible from the center hub. The damage was induced three times by wrapping the boom specimens to different length, as shown in Figure 15. Before any damage was introduced to the boom specimen, baseline sensing data was collected. Stage 1 was wrapping the specimen around the hub to introduce damage up to the section indicated. The modal analysis was conducted after that. In the second step, both stages 1 and 2 were used and in step 3, stages 1, 2 and 3 were all used to introduce damage to the boom structure.

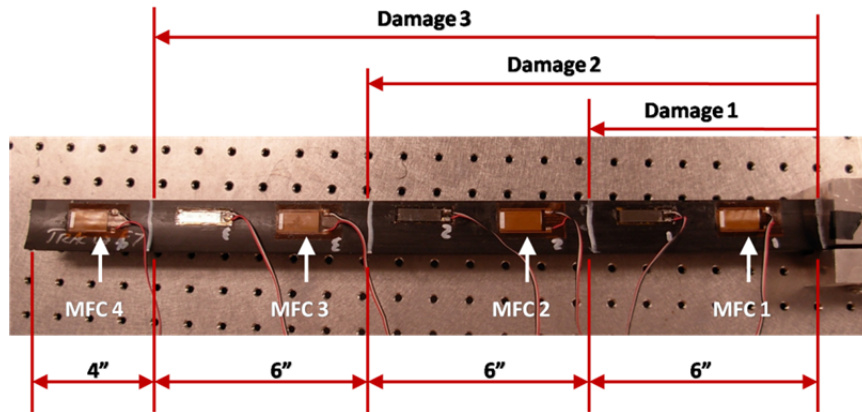


Figure 13. The composite boom specimen



a) The initial position of the composite boom

b) The wrapped composite boom

Figure 14. The composite boom wrapping machine

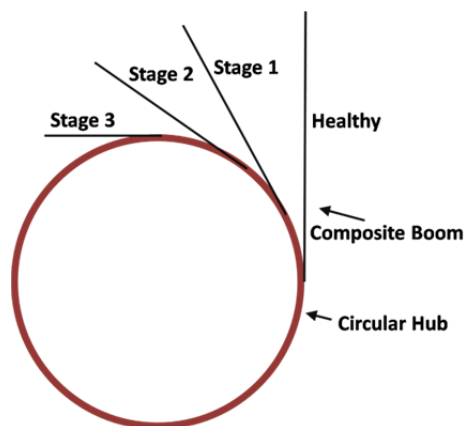


Figure 15. Three damage stages for the composite boom flattening/wrapping test.

Current NDE techniques, such as thermography and ultrasonic scan, cannot detect matrix microcracking in composites. However, matrix microcracking and structural stiffness degradation can be detected by the shift of resonant modes using vibration

modal analysis. In order to validate the matrix microcracking induced by flattening and wrapping of the boom, the first three resonant modes were measured experimentally through a scanning head laser vibrometer (Polytech Inc., model: VCS-310) coupled with a vibration shaker. The experimental setup of vibration modal analysis is shown in Figure 16. Three steps were used to ensure the laser points were in the exact locations during each scan. First, the length from the free end of the boom to the custom made fixture was the same in each scan. Then, the sample was clamped at the same position on the shaker according to the marks drawn on the shaker fixture. Finally, the vibrometer scan head was fixed and the position of boom on the shaker was adjusted so that each scan was started from the same point, as shown in Figure 16. The shift of second resonant mode can be seen in Figure 17. The second resonant mode shows the clearest shift after damage is induced into the specimen.

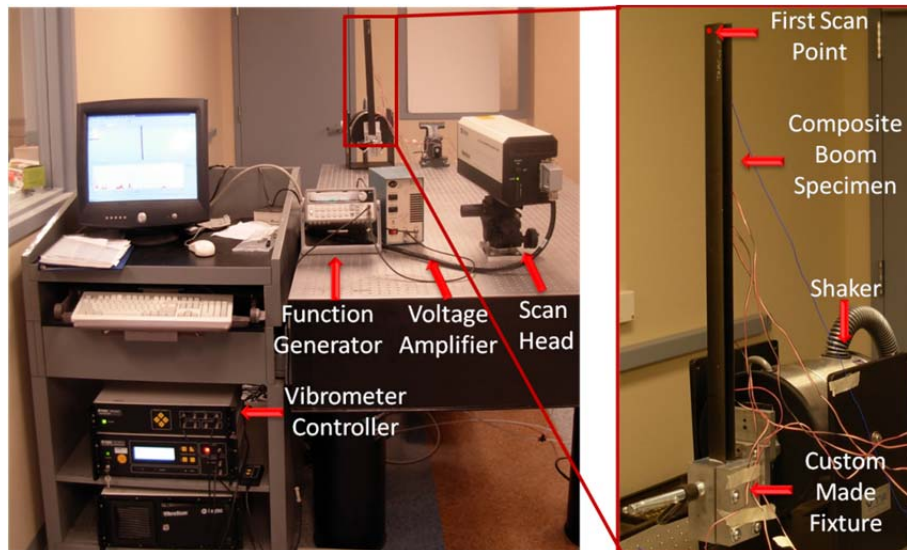


Figure 16. Experimental setup of vibration modal analysis

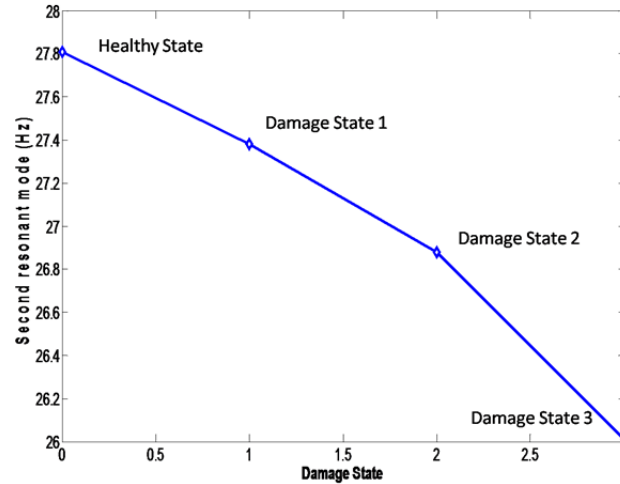


Figure 17. The resonant mode shift

A broadband sweep signal with frequency varying from 10 Hz to 1 kHz is used for active sensing of MFCs and the excitation signal collected from MFC 1 (Figure 13) is shown in Figure 18 a. A representative sensor signal from MFC 4 (Figure 13) at a healthy state condition is shown in Figure 18 b. The power spectral density plots of both the input and output signals at healthy and three damage states are shown in Figure 19. With constant input signals, the differences of the power spectral density at different damage states were not very clear. Frequency response method and ARX model were used for more sensitive and robust damage detection.

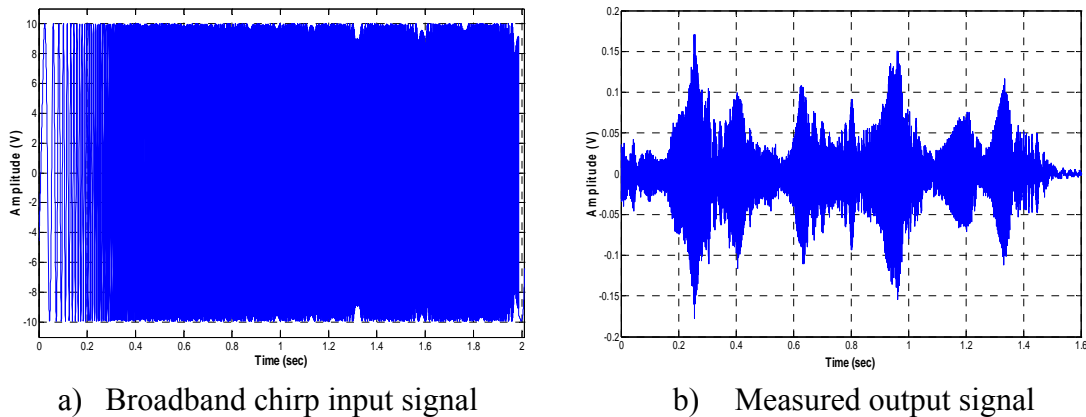


Figure 18. Excitation/sensor signals and their power spectral density plots for MFC1a) and MFC4 b)

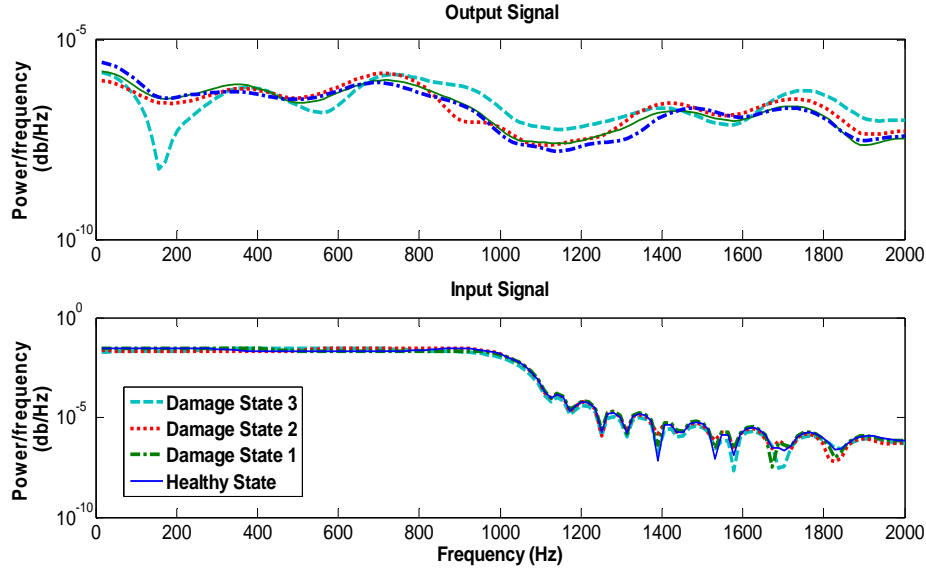


Figure 19. The power spectral density of input and output MFC1 and MFC4 signals at different damage states

4.2 Results and Discussion

4.2.1 Frequency Response Method of Input-output MFC Transducers

The frequency response method can be used to analyze the input/output relationship and to non-parametrically understand the key aspects of the system before moving to the more complex parametric modeling stages. The information obtained is the basis for identifying parametric transfer function models. In this paper, a SISO frequency response method is used to analyze the change of transfer functions at different damage states. The input signals are collected from MFC 1(Figure 13) and output signals are collected from MFC 4 (Figure 13). The sensors input/output signals cover the entire damage area and can be used for global damage characterization. The amplitude and phase plot versus frequency, which can be calculated using Eq. 10)-14), are showed in Figure 20.

In Eq. 12 the frequency response is determined from the ratio of the cross-correlation spectrum estimate, S_{yx} , and auto-correlation spectrum estimate, S_{xx} . The output measurement noise is uncorrelated with the prescribed excitation input. As described before, the amplitude change of the frequency response at relatively low frequency range (from 10 Hz to 200 Hz) is mainly caused by the presence of nonlinear properties when matrix cracks are introduced. The understanding of nonlinearity in damaged composite structures helps to choose the proper model for the transfer function estimation and design the damage index based on the estimated damage index.

The frequency response method provides an approach to select frequency ranges for the input/output pair to include only relevant data. As shown in Figure 20, the

amplitude has a clear response at a low frequency range from 10 Hz to 200 Hz. The phase response is more obvious above 100 Hz. This quick analysis helps to choose the frequency range, which provides useful data for the transfer function estimation.

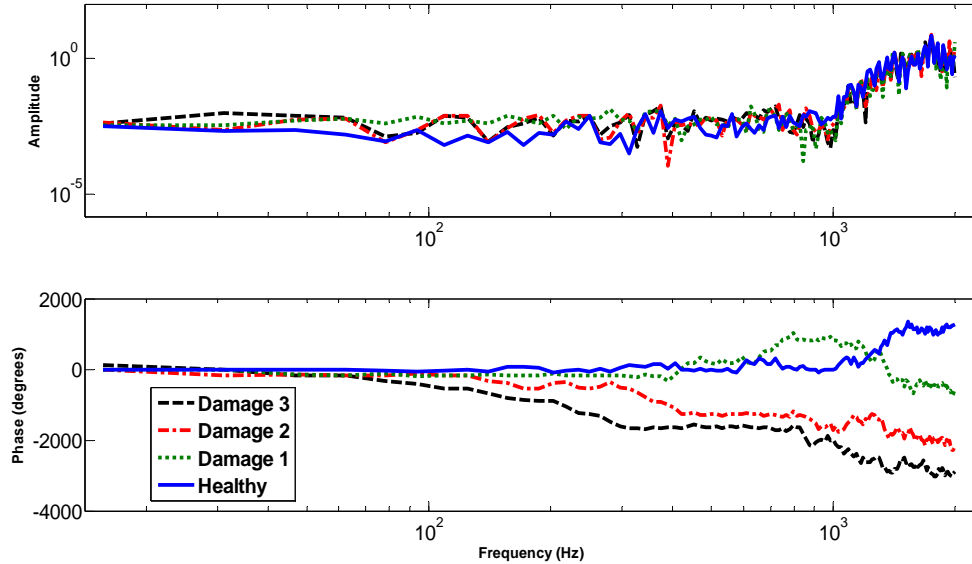


Figure 20. The frequency response of input/output signal measured from MFC1 and 4

A key aspect for frequency response method is the direct and accurate identification of time delays. The linear relationship between the time delay τ and frequency response phase shift with frequency, ω (rad/s), is expressed as:

$$\varphi = -\tau\omega \quad (29)$$

where φ is the angle of phase shift at frequency, ω (rad/s). From the frequency response plot shown in Figure 20, the phase shift at different damage states is the clearest feature, especially over the frequency range of 100 Hz to 1 KHz. This indicates that the time delays are more significant in the relatively high frequency range as more damage is introduced. The time delay feature is not only useful for transfer function estimation, but can also be used for stiffness estimation for damage propagation.

4.2.2 Transfer Function Estimation and Order Selection of ARX Model

By carefully choosing the order of ARX model, SISO transfer function can be estimated accurately and efficiently. As shown in Eq. (27), the order of ARX model is the sum of the order of output n and the order of input m . The value of m and n can be different. The criterion of selecting proper order number is to get the reasonable estimation with the smallest order number. In order to find the optimized order number, a set of estimations is needed. Experimental measurements from MFC 1 and MFC4 (Figure 13) at the healthy state are used as input/output pair for the order analysis. As the order number increases, the estimation error decreases, as shown in Figure 21. The sum of m and n is the main influence of the estimation error, but each value of m and n

is also considered in order to get the minimized order number. Although the estimation accuracy can be improved with a high order ARX model, the calculation cost increases dramatically. Finally, ARX (28,12) is chosen for the ARX model.

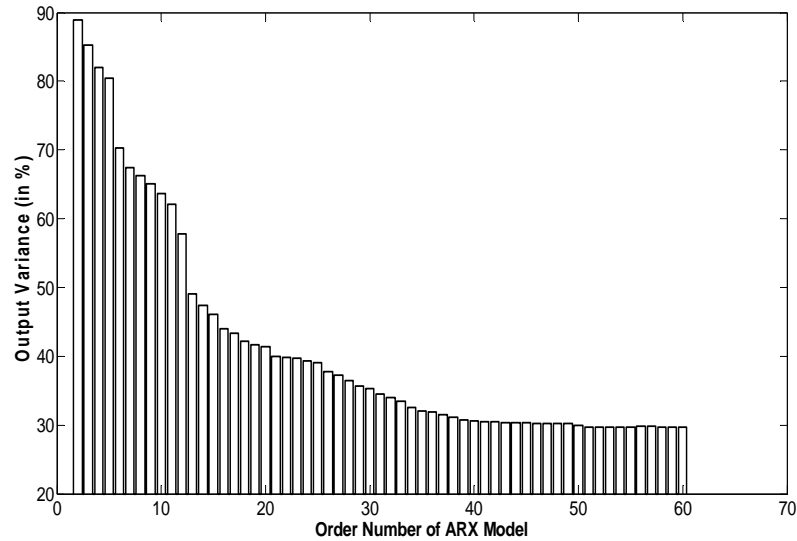


Figure 21. Estimation error with different order number

To check the estimation accuracy of the chosen model, one pair of experimental input/output signals collected from MFC 1 and 4 was used to train and validate the ARX (28,12) model. The first half of the signal in the time domain is used to train the model and the second half measured output is compared with the simulated output. The comparison of simulated output signal and experimental output signal can be seen in

Figure 22. By carefully choosing the model order, ARX (28,12) model is able to accurately simulate output signal.

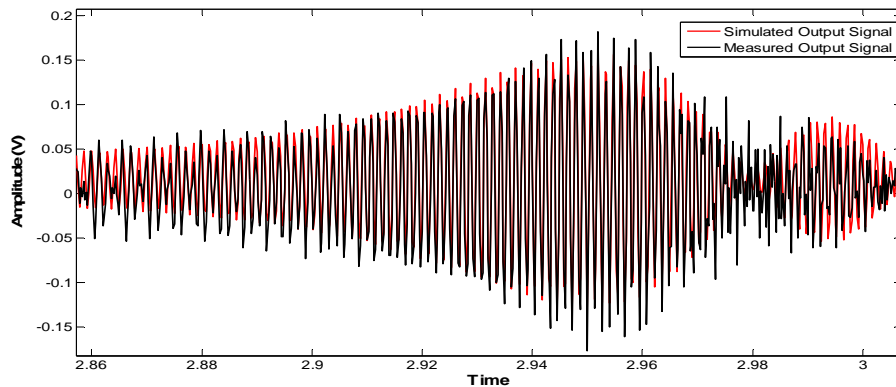


Figure 22. Comparison of simulated signal and experimental signal (zoomed)

4.2.3 Damage Identification Using Damage Index

To evaluate the damage state of the entire composite boom specimen subject to flattening and wrapping around the circular hub, both global damage estimation and local damage estimation are completed. Global damage estimation uses MFCs 1 and 4 (Figure 13), which cover the entire boom. The damage index obtained from global damage estimation showed the average damage condition along the entire boom. In Figure 23, the estimation starts from the healthy state at which the damage index is zero. However, as the flattening and wrapping induced matrix cracks into the boom, the damage index grows gradually. Global damage state estimation provides a clear trend of damage growth. However, more damage accumulates in the section between MFC 1 and 2, as this area has been wrapped three times during the experiment. Global damage state estimation cannot highlight such local damage states. In order to concentrate on the hotspot between MFCs 1 and 2, local damage estimation analysis is used. The local damage state estimation for the section between MFCs 1 and 2 is shown in Figure 24. Compared with the global estimation results in Figure 23, local damage state estimation is more sensitive to damage. The reason is the first two damage states contain both of healthy and damage sections in the analysis area. This increases the estimation error $\varepsilon_0(t)$ at healthy state. The sensitivity of the damage index decreases as long as the reference becomes larger. Generally speaking, the damage index should provide more sensitivity for local damage state estimation.

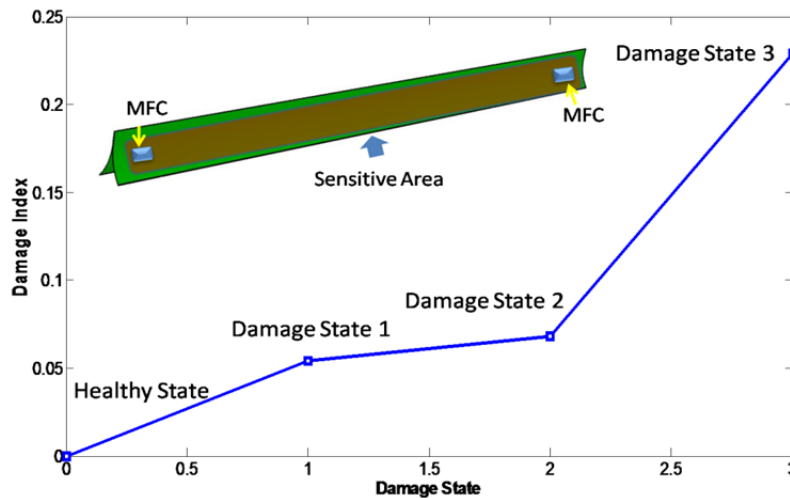


Figure 23. The global damage estimation

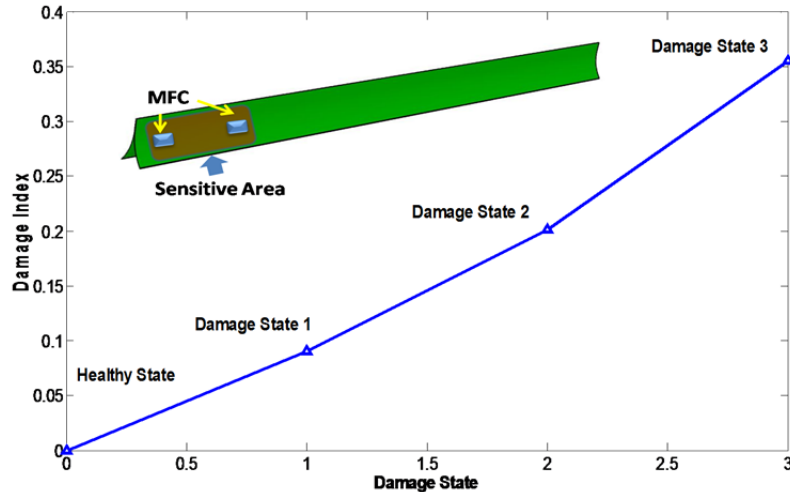


Figure 24. The local damage estimation between MFC1 and 2

4.3 Conclusions

The system identification techniques based SHM approach was proposed to investigate matrix cracking damage in composite booms subject to flattening and wrapping around a circular hub. Both the frequency response method and ARX model are used to perform SISO transfer function estimation and damage state identification. A flexible MFC actuator excites the other three MFC sensors using low frequency sweep signals to provide experimental input/output data. The frequency response method is used to non-parametrically analyze the relationship between input/output sensor signals and select a significant frequency range. It also provides guidance for the transfer function analysis using the ARX model. The order of the ARX model is decided by considering both the estimation accuracy of the model and the calculation cost, and the ARX (28,12) model is chosen. The order selection of ARX model is validated by comparing the simulated and experimental output signals. The damage index estimation using the residual error of the ARX model provides a clear trend of damage growth because the composites will present nonlinear structural properties when matrix cracks are introduced. The newly defined damage index is more sensitive in a small analysis area, but still provides decent estimation for the entire damage booms.

5.0 TASK 3 REPORTING

This task addressed the development of an integrated Structural Health Monitoring (SHM) system for damage diagnosis, including detection and localization, in a complex composite structure. A lamb wave based active sensing method for damage diagnosis is investigated first. The propagation of Lamb waves in a stiffened carbon fiber polymer matrix composite panel is then characterized. A two step damage detection and characterization approach, which uses both pulse-echo and pitch-catch active sensing schemes, is presented for the identification of delaminations in the stiffened composite panels. The Matching Pursuit Decomposition (MPD) algorithm is used for the representation of the sensor signals in the time-frequency domain. The delaminations are detected by identifying the converted Lamb wave modes in the time-frequency domain. The MPD algorithm is further used to assess the delamination location in composite structures. The sensor locations and differences in Time-of-Flight (ToF) are used to formulate three nonlinear equations. The nonlinear equations are converted into an unconstrained optimization problem and solved using the Newton's method. Due to the redundancy of the PZT sensor array, a probabilistic location estimation algorithm is used to estimate the confidence range of the delamination in the composite structures.

5.1 Method, Assumptions, And Procedures

5.1.1 Time-Frequency Representation of Lamb Wave using MPD

Lamb wave propagation is complicated by wave dispersion, boundary reflections and mode conversions. To accurately identify each Lamb wave mode and extract information to localize delamination, an advanced time-frequency analysis method is required. The MPD algorithm is used as the time-frequency analysis method to calculate the difference of ToF between sensors in this project.

For Lamb waves, the signal with finite energy, $s(t)$, can be decomposed into a linear combination of time-frequency atoms. This type of infinite approximations can be written as,

$$s(t) = \sum_{i=0}^{\infty} \beta_i g_i(t) \quad (30)$$

where $g_i(t)$ is the time-frequency atom (sub-waveform) selected from the MPD dictionary A and β_i is the corresponding expansion coefficient. The finite linear combination of these time-frequency atoms can be used to provide an approximation of the signal with high accuracy. After N iterations, the resulting expansion can be expressed as,

$$s_N(t) = \sum_{i=0}^N \beta_i g_i(t) \quad (31)$$

The residual signal $Rs_N(t)$ with N iterations is,

$$Rs_N(t) = s(t) - s_N(t) = s(t) - \sum_{i=1}^N \beta_i g_i(t) \quad 32)$$

Because the signal has finite energy, the energy of the approximated signal is also preserved. The energy conservation can be expressed as,

$$\|s(t)\|^2 = \sum_{i=0}^N \|s_N(t)\|^2 + \|Rs_N(t)\|^2 \quad 33)$$

In order to find the best match between the signal and time-frequency atoms, the inner product of the signal and each time-frequency atom is calculated. Let $g(t) \in A$, where the signal, $s(t)$, can be decomposed into wavelets as shown by,

$$s(t) = \langle s(t), g(t) \rangle g(t) + Rs \quad 34)$$

where Rs is the residual signal after approximation using the time-frequency atom, $g(t)$. To minimize the energy of Rs , the proper $g(t)$ is defined to satisfy the equation,

$$|\langle s(t), g(t) \rangle| \geq \beta \sup |\langle s(t), g(t) \rangle| \quad 35)$$

where β is an optimality factor that satisfies $0 < \beta \leq 1$, $\sup |\langle s(t), g(t) \rangle|$ is the least upper bound of the inner product of $\langle s(t), g(t) \rangle$. The decomposition of signal $s(t)$ is completed by successive calculation with time-frequency atoms from the dictionary. Let $g_i(t)$ be the time-frequency atom of the i^{th} iteration, and the approximated signal at this iteration is,

$$s_i(t) = \langle Rs_i(t), g_i(t) \rangle \quad 36)$$

when $i=0$, let $Rs_0 = e(t)$, the approximated signal with a total of N iterations is,

$$s_N(t) = \sum_{i=1}^N \langle Rs_i(t), g_i(t) \rangle \quad 37)$$

and the original signal can be expressed as,

$$s(t) = \sum_{i=1}^N \langle Rs_i(t), g_i(t) \rangle + Rs_N \quad (38)$$

where Rs_N is the residual signal at the N^{th} iteration. Although a redundant dictionary can provide flexible decomposition of the signal, the computational cost is consequentially high. To reduce the number of unnecessary time-frequency atoms, a modified MPD algorithm is used. The time-frequency dictionary of the MPD algorithm is optimized based on the features of the Lamb wave signals from the structures being interrogated. Limited sub-waveforms which can best represent the original signal are included in the dictionary. By using the optimized atom dictionary, the original signal can still be efficiently decomposed with high local time-frequency resolution.

The actuation signal used in the experiments conducted here is a cosine burst wave. According to the Lamb wave theory, only S_0 , A_0 and the related converted modes exist as sub-waveforms. These sub-waveforms can be expressed as,

$$s(t) = e^{-\beta t^2} \cos(2\pi ft) \quad (39)$$

where the constant β defines the width of the burst wave and f is the central frequency. S_0 , A_0 and the related converted modes can be obtained by the dilation and translation of the basic sub-waveform. This procedure reduces the size of the MPD dictionary significantly. It must be noted that the MPD algorithm efficiently yields a compact representation of the burst wave signals in terms of selected basic atoms in the dictionary. Therefore, it reduces the computational cost significantly. In addition, the noise is filtered out because the noise waveforms are typically orthogonal to the selected atoms.

Using the refined MPD algorithm, the guided wave signals from different sensors can be represented in the same time-frequency domain. The difference of ToFs between sensors can be compared and accurately calculated. This ToF information is used as input to damage location formulation.

5.1.2 Experimental Setup

Four carbon fiber polymer matrix composite panels with $[0^\circ/90^\circ/0^\circ]_s$ layup were fabricated in-house. Each panel has two co-cured blade stiffeners on its surface, as illustrated in Figure 25. Plain weave carbon fiber fabrics were used as the fiber reinforcement. The epoxy FS-A23 (resin) and FS-B412 (hardener) (from Epoxy System Inc.) were used as the matrix system. A total of nine PZT wafers and one PZT ring were surface bonded on the stiffened side of the panel surface. The dimensions of the structure and the locations of the PZTs are shown in Figure 26. Two composite panels were fabricated with seeded delaminations. Two Teflon patches were inserted during lay-up to generate delaminations. The other two composite panels were fabricated without delaminations to study the healthy state of the composite panels. A flash

thermography (Thermal Wave Imaging Inc., Model: EchoTherm) system was used to visualize the delaminations as seen in Figure 27. A waveform was generated using the NI 5412 waveform generator, and the Lamb wave signals were captured using the NI 5105 digitizer at the sampling frequency of 20 MHz. In order to optimize the central frequency of the actuation signal, several actuation signals were generated using central frequencies varying from 10 to 300 kHz in 10 kHz increments. Ten observations were recorded at each frequency and the sensor signal was averaged from these observations to reduce the sampling error.

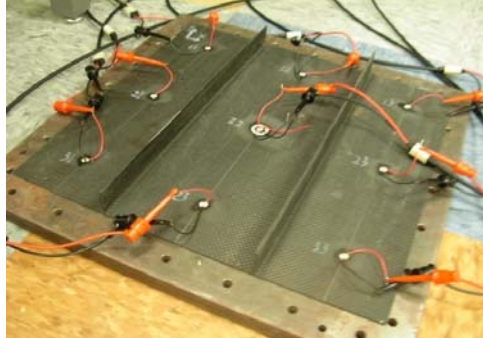


Figure 25. Stiffened composite panel with bonded PZT patches

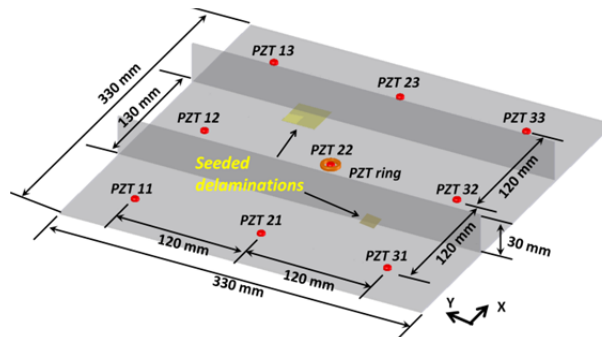


Figure 26. Dimensions of the composite panel and PZT patches

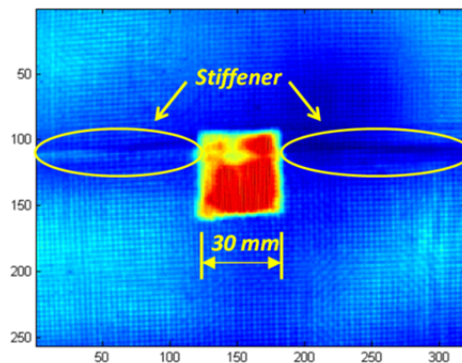


Figure 27. Flash thermography image of composite stiffened panel with $30 \times 30 \text{ mm}^2$ delamination

5.2 Results and Discussion

5.2.1 Group Velocity Calculation

Most Lamb wave approaches, such as mode decomposition and the ToF calculation, require the group velocity of each Lamb wave mode. Group velocities of S_0 and A_0 Lamb wave modes are the most basic parameters used in Lamb wave analysis. Theoretically, the group velocity at any frequency can be calculated and illustrated using dispersion curves. However, due to the material complexity, group velocities of S_0 and A_0 modes are calculated using experimental data. PZT 22 was used as the actuator and PZTs 12 and 32 were used as the sensors. The signal recorded from PZT 12 is shown in Figure 28 (a). Due to the size limitation of the sample, the first two Lamb wave packages (S_0 mode and the S_0 reflection mode) overlap in the time domain. It is difficult to calculate the ToF of the S_0 mode because the center of S_0 mode cannot be localized. However, the TFR of the sensor signal clearly represents the first three Lamb wave packages in the time-frequency domain, as shown in Figure 28 (b). Because the propagation distances are known, these three Lamb wave packages can be identified as the S_0 mode, S_0 reflection mode from the boundary and the A_0 mode. Similar results can be obtained by studying the data recorded from PZT 32. Therefore, the group velocities of S_0 and A_0 modes can be accurately calculated as 5250 m/s and 1470 m/s, respectively.

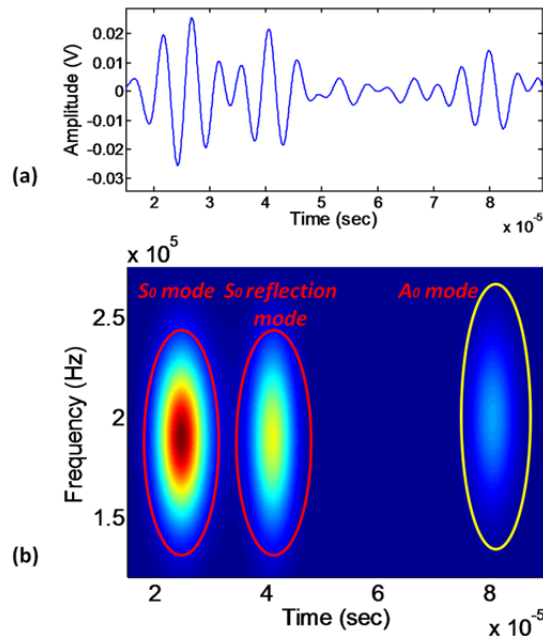


Figure 28. (a) Signal of the Lamb wave recorded from PZT 12; (b) TFR of the Lamb wave recorded from PZT 12

The angular dependence of Lamb wave propagation is studied by comparing the velocities of the S_0 mode along all the possible actuator-sensor paths. When PZT 11 was used as the actuator, five possible paths are between the 0° and 90° range. It is noted that since the composite panel was fabricated using plain weave fiber fabric, and the fiber fabric structure in the 0° and 90° are the same, the velocity of S_0 at 0° and 90° are

the same. The S_0 mode's group velocity at each detectable angle is shown in Figure 29. It is observed that at 0° , the S_0 mode has the highest propagating velocity (5.25 m/ms). At 45° , the S_0 mode has the lowest propagating velocity (4.01 m/ms). The S_0 mode's group velocity at different angles is used to identify the arrival and reflection of the S_0 mode in the Lamb wave decomposition for damage identification in the following section.

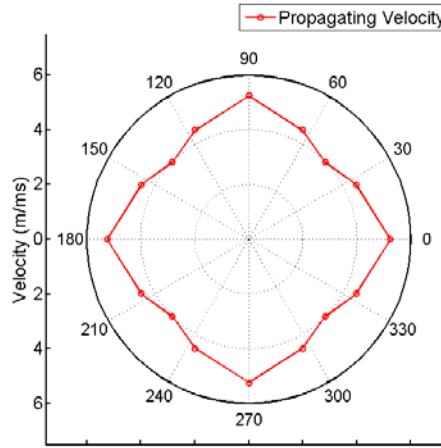


Figure 29. Angular dependence of wave propagating velocity (S_0 mode) in the composite panel

5.2.2 Lamb Wave Attenuation

Wave attenuation is defined as the reduction of signal amplitude with the propagation distance. It is a critical feature for the effectiveness of damage detection using Lamb wave techniques. The attenuation rate of a Lamb wave signal is a function of the wave frequency and the propagation distance, which can be expressed as,

$$A \sim F(f, d) \quad (40)$$

where A is the attenuation rate of individual Lamb wave signal with a frequency f and a propagation distance, d , respectively.

Lamb wave attenuation is studied using the composite panels with seeded delaminations. PZT 22 was used as the actuator. Lamb wave signals collected from PZT 12 and PZT 21 are analyzed to study the influence of the blade stiffener on the propagation of Lamb waves. The first received S_0 mode can be easily isolated from the other Lamb wave modes because it has the highest group velocity. Therefore, the first measured S_0 mode can be used to determine the wave attenuation. More severe wave attenuation is observed when Lamb waves propagate through stiffeners, as shown in Figure 30. The horizontal axis represents the ToF of the first arrived S_0 mode from the actuator to the sensor. The amplitude plotted on the vertical axis demonstrates the reduction of wave amplitude. It is observed that the amplitude of the S_0 mode collected

from PZT 21 is 57% of that recorded from PZT 12. The results indicate that the presence of stiffeners significantly reduces the energy of the Lamb wave. The signals collected from PZT 31 and 13 are used to study the influence of the delamination sizes on the propagation of Lamb waves. As shown in Figure 31, the amplitude of the S_0 mode reduced more severely when it propagated through a larger delamination area. It is observed that the amplitude of the S_0 mode collected from PZT 31 is 55% of that recorded from PZT 13. The delamination size has a significant influence on the Lamb wave attenuation.

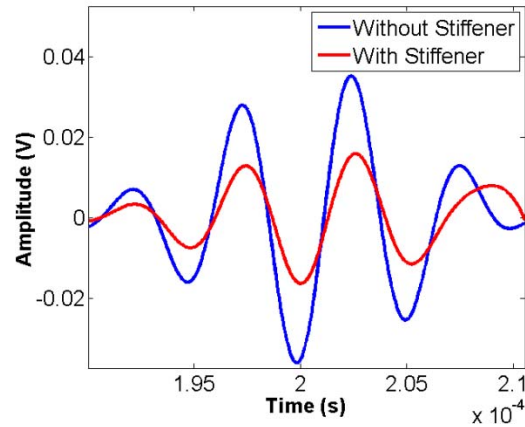


Figure 30. Wave attenuation of the S_0 mode from PZT 12 and PZT 21

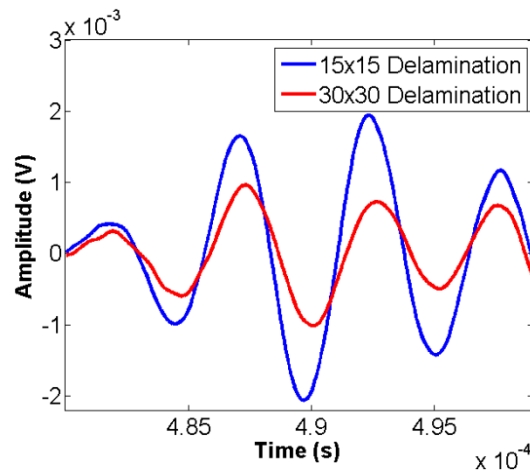


Figure 31. Wave attenuation of the S_0 mode from PZT 13 and PZT 31

The wave amplitude represents the signal energy at a specific instant. The reduction of signal energy can be used to illustrate the wave attenuation for the whole signal. The signal energy can be expressed as,

$$E(s) = \int s^2(t)dt \quad \text{.....41)}$$

where $E(s)$ is the energy of signal $s(t)$. By calculating the energy of signals recorded from each PZT sensor, the influence of the stiffener and delamination can be clearly

illustrated. When PZT 22 was used as the actuator, the signal energy was normalized by the largest sensor signal. It is observed that signal from PZT 32 has the largest energy, so the normalized signal energy of PZT32 is 1. The other signal energies are calculated accordingly. Figure 32 shows the normalized signal energy collected from all the PZT sensors (noted below sensor in Figure 32). Since there is no stiffener or delamination between the actuator and PZTs 12 and 32, the signals recorded from the two PZTs have similar amount of energy. The stiffeners most significantly influence the signals recorded from PZTs 21 and 23. The signal recorded from PZTs 11 and 33 also were only influenced by the stiffeners. However, due to the longer propagation distances and the angel between fiber orientation and wave propagation direction, the signals from PZT 11 and 33 showed more energy loss than PZT 21 and 23. For PZTs 31 and 13, both the stiffeners and delamination caused the severe energy loss. A larger energy loss from PZT 31 correlates to a larger delamination size.

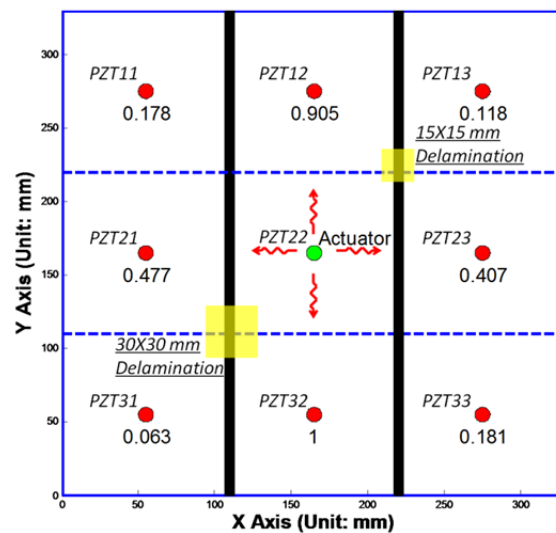


Figure 32. Normalized PZT sensor signal energy

5.2.3 Global Damage Detection using Pulse-Echo Scheme

Pulse-echo scheme is first used to detect the existence of delamination. The composite panel's complex geometry introduces several reflection modes to the sensor signal when the pulse-echo scheme is used for damage detection. To successfully detect delamination, the different reflection modes need to be isolated and identified. When the S_0 mode arrives at the T-section of the blade stiffener, the mode scatters into three components, one propagating in the plate, one propagating in the blade stiffener and a reflection in the plate, as shown in Figure 33 (a).

Similarly, when the component of the S_0 mode that is transferred into the blade stiffener reflects back to the T-section, this mode also scatters into another three components. Two of these propagate along different directions in the plate and the third is reflected back into the stiffener, as shown in Figure 33 (b).

Due to the Lamb wave scattering at the T-section, the S_0 and A_0 modes generated by the actuator propagate along different possible paths and finally are recorded by the PZT ring sensor. The eight shortest possible Lamb wave propagation paths are shown in Figure 33 (c). Both the propagation distance and the group velocities of S_0 and A_0 modes are known, therefore the theoretical ToF along each propagation path can be calculated, as shown in Table 1 and 2. Since PZT 22 is placed in the center of the panel, path 6 is the same in both the X and Y directions. Therefore, path 6 will contain Lambs waves from both the X direction and Y directions, which results in an increase in magnitude.

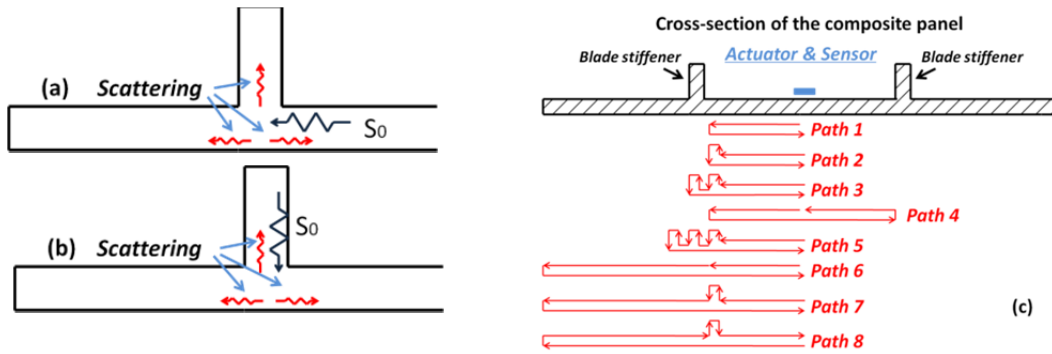


Figure 33. (a) Lamb wave mode scattering into T-section; (b) Lamb wave mode scattering out of T section; (c) The different paths of Lamb wave propagation in the stiffened composite panel using the pulse-echo approach

Table 7. The ToF analysis for the S_0 mode

	<i>Path Distance (m)</i>	<i>Group Velocity of S_0 mode (m/ms)</i>	<i>Time of Flight (ms)</i>
<i>Path 1</i>	0.13	5.25	0.0248
<i>Path 2</i>	0.19	5.25	0.0362
<i>Path 3</i>	0.25	5.25	0.0476
<i>Path 4</i>	0.26	5.25	0.0495
<i>Path 5</i>	0.32	5.25	0.0610
<i>Path 6</i>	0.33	5.25	0.0629
<i>Path 7</i>	0.39	5.25	0.0743
<i>Path 8</i>	0.39	5.25	0.0743

Table 8. The ToF analysis for the A_0 mode

	<i>Path Distance (m)</i>	<i>Group Velocity of S_0 mode (m/ms)</i>	<i>Time of Flight (ms)</i>
<i>Path 1</i>	0.13	1.47	0.0884
<i>Path 2</i>	0.19	1.47	0.1292
<i>Path 3</i>	0.25	1.47	0.1700
<i>Path 4</i>	0.26	1.47	0.1768
<i>Path 5</i>	0.32	1.47	0.2176
<i>Path 6</i>	0.33	1.47	0.2240
<i>Path 7</i>	0.39	1.47	0.2653
<i>Path 8</i>	0.39	1.47	0.2653

In Figure 34, the S_0 mode conversion is considered when an S_0 wave mode arrives at the stiffener. Mode conversion occurs at the T-section because of the thickness change. The original S_0 mode converts into A_0 and S_0 modes and propagate along the 3 possible directions. Due to the low group velocity of the A_0 mode, only the converted A_0 mode reflected back to the PZT ring sensor was recorded in the experiment. However, the reflected converted A_0 mode cannot be clearly displayed in the TFR because of the low energy caused by wave scattering and attenuation.

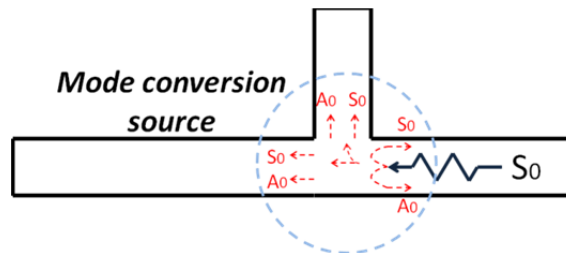


Figure 34. Mode conversion in T section

The healthy composite panel is used to identify each Lamb wave mode for the echo signal. A burst wave with a central frequency of 180 kHz was used to generate the Lamb wave. The Lamb wave echo signal was recorded from the PZT ring sensor. The TFR of the echo signal is shown in Figure 35. The first two atoms can be easily identified as the S_0 mode propagates along paths 1 and 2, respectively. The experimental ToF of the two atoms matches with the theoretical calculation. Since paths 3 and 4 have close path lengths, the S_0 modes propagating along the two paths overlap together in the time-frequency domain and represent as the third atom in Figure 35. Similarly, the S_0 modes propagating along paths 5 and 6 merges and is seen as the fourth atom in Figure 35. The fifth atom is identified as the A_0 mode since the experimental ToF of this mode matches with theoretical calculation shown in Table 2. The theoretical and experimental results for ToF are compared in Table 3. Due to the signal attenuation and multiple reflections and scatterings, it is noted that the S_0 mode propagating along paths 7 and 8 loses most of the signal energy. There is no clear TFR for this mode in the time-

frequency domain. It can be reasonably concluded that the S_0 mode, which propagates longer than path 7 and 8, can be ignored.

Table 9. The ToF comparison for the S_0 modes

	<i>Theoretical Time of Flight (ms)</i>	<i>Measured Time of Flight (ms)</i>
<i>Path 1</i>	0.0248	0.0248
<i>Path 2</i>	0.0362	0.0365
<i>Path 3</i>	0.0476	0.0499
<i>Path 4</i>	0.0495	0.0499
<i>Path 5</i>	0.0610	0.0615
<i>Path 6</i>	0.0629	0.0615

Delamination was detected in the damaged composite stiffened panel. Using the MPD time-frequency analysis algorithm, the TFR of the echo signal can be demonstrated, as shown in Figure 36. Compared to the TFR shown in Figure 35, the S_0 mode propagating along path 1-6 and the A_0 mode can be identified at the same time instance. In addition, one more atom is detected in this TFR. When the S_0 modes propagate through the delamination of the composite panel, the two modes convert into a new mode, which can be named as the MC mode. In fact there are several MC modes due to multiple delaminations. After several reflections of the stiffeners and boundaries, the MC modes overlap and combine with each other. This combined MC mode is recorded by the PZT ring sensor. The new atom correlates with the delaminations in the composite panel. Using the global pulse-echo scheme, the delaminations can be quickly detected by one single PZT ring sensor. However, the pulse-echo approach cannot provide more information about the location, number of delaminations, etc. A local pitch-catch active sensing scheme is necessary to obtain these details.

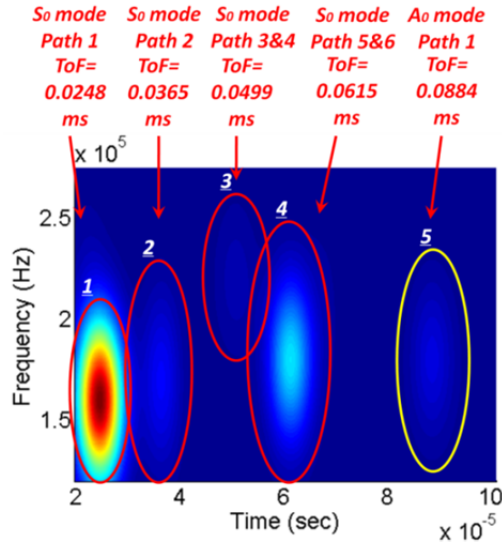


Figure 35. TFR and mode identification of the echo Lamb wave in the healthy stiffened panel

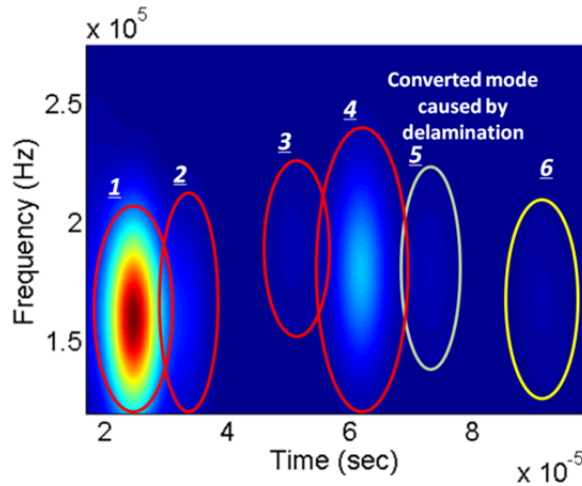


Figure 36. TFR and mode identification of the echo Lamb wave using the stiffened panel with delamination

5.2.4 Local Damage Detection using Pitch-Catch Scheme

Once delamination is detected using the global scheme, local damage detection approach is used to find more detailed damage information. The pitch-catch scheme uses a sensor array with nine PZT wafers to detect the local delamination between the actuator and sensors. PZT 22, which is located at the center of the composite panel, is used as the actuator. A burst signal with a central frequency of 180 kHz is used as the excitation signal. The PZT sensor signal recorded from the healthy panel is used as the baseline data. The first five Lamb wave atoms in the TFR are identified using the

baseline data. Delamination is detected by identifying the new MC modes in the signal recorded from the panel with delaminations, which is similar to the pulse-echo approach.

Using the healthy composite panel, the sensor signal collected from PZT 21 is used to study the influence of the stiffened panel on the sensor signal. The first four possible propagation paths for PZT 21 are shown in Figure 37, and the associated TFR is shown in Figure 38. The first S_0 and the following reflection of S_0 modes are illustrated. The arrival of the A_0 mode was recorded at 0.086 ms. The experimental ToF results matches with theoretical analysis. Similar time-frequency atoms with more attenuation and time shift can be identified in the signal collected from the other PZT sensors.

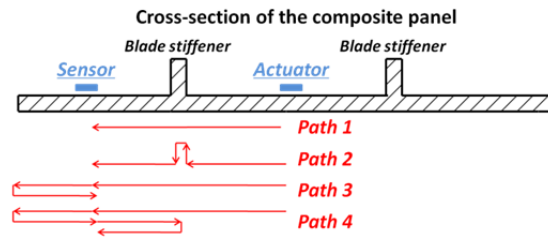


Figure 37. Possible propagation paths for PZT 21

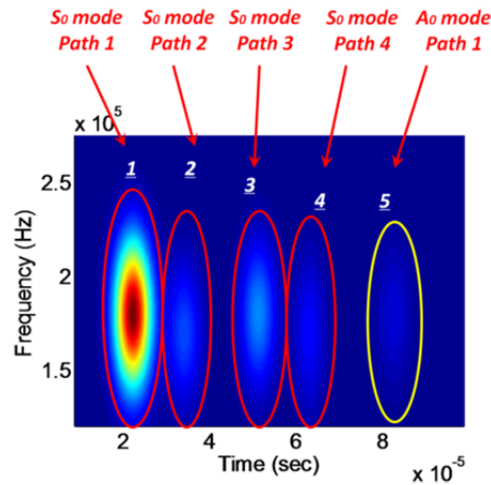


Figure 38. TFR of Lamb wave collected from PZT 21 using a healthy panel

Two delaminations were detected between PZTs 22 and 31 and PZTs 22 and 13. The TFR of the sensor signal recorded from PZT 31 using the healthy panel is shown in Figure 39. Each Lamb wave mode can be represented as a time-frequency atom in the TFRs. The location of each atom in the TFR can be verified by studying the ToF of each Lamb wave mode. As shown in Figure 39, the first time-frequency atom is identified as the first arrived S_0 mode, the second and the third atoms are the S_0 reflection modes due to the boundary and the stiffener. The fourth atom is the A_0 mode. Similar atoms can be identified in the sensor signals recorded using the composite panels with seeded delaminations. However, using the damaged composite panel, the fifth atom in the TFR of the PZT 31 signal is identified as the converted mode caused by the delamination, as

shown in Figure 40. Due to the delamination between PZTs 22 and 13, the converted mode is also detected in the signal recorded from PZT 13. However, in the sensor signals of PZTs 11 and 33, there is no such converted mode introduced by delamination. These results demonstrate that the two seeded delaminations are detected by the local PZT sensor using the pitch-catch active sensing scheme. Using the developed methodology, multiple delamination damages can be detected.

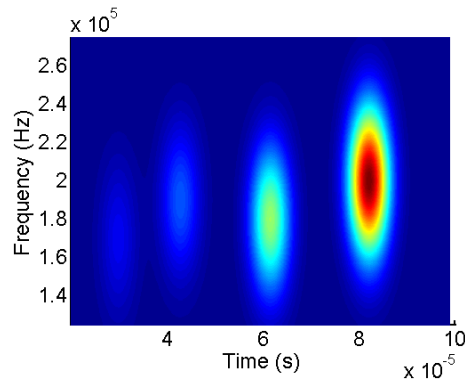


Figure 39. TFR of Lamb wave collected from PZT 31 using a healthy composite panel

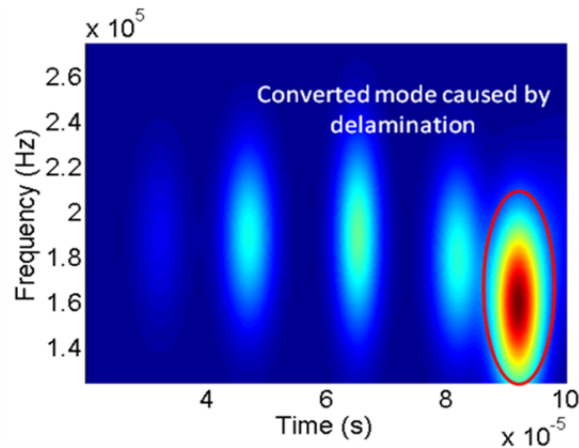
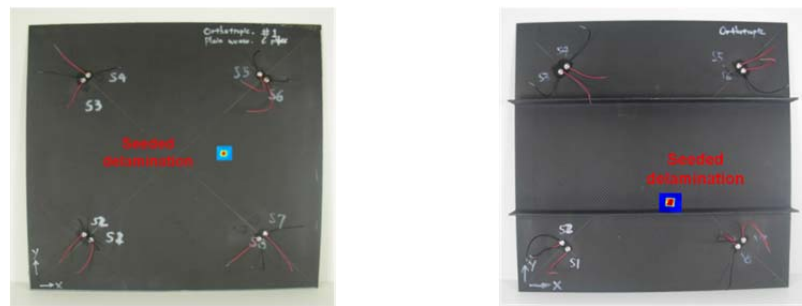


Figure 40. TFR of Lamb wave collected from PZT31 using composite panel with delaminations

5.2.5 Damage Localization Using Time-Frequency Analysis

The developed damage localization methodology is validated by three experiments conducted with carbon fiber reinforced composite samples. In experiment 1, composite plates with a $[0^\circ]_6$ layup were fabricated in-house. Plain weave fiber fabrics were used as the fiber system to simulate composites with quasi-isotropic material properties. In

experiment 2, composite plates with $[(0^\circ)_3 \text{ pw}/90^\circ \text{ uni}/(0^\circ)_3 \text{ pw}]$ layup were fabricated. Both plain weave fiber fabrics and unidirectional fiber fabrics were used to obtain orthotropic material properties. In experiment 3, stiffened composite panels with two stiffeners were fabricated using $[0^\circ]_6$ layup. Plain weave fiber fabrics were used as the fiber system. A two-part epoxy, FS-A23 (resin) and FS-B412 (hardener) from Epoxy System Inc., was used as the matrix system for all composite coupons. Delaminations were seeded in the composite plates and panels during fabrication using Teflon patches. Flash thermography (Echo Therm System) was used to validate the position and size of the delaminations. The composite plates and stiffened panels with flash thermographic images are shown in Figure 41.



(a) Composite plate

(b) Stiffened composite panels

Figure 41. Composite plates and stiffened panels used in experiments

A PZT array using eight PZT transducers were bonded on the surface of the composite samples in four pairs, as shown in Figure 41. In each PZT pair, the two transducers were placed close to each other. One PZT was used as the actuator and other three PZT pairs were used as sensors. A waveform was generated using a NI 5412 waveform generator, and the Lamb wave signals were captured using an NI 5105 digitizer at a sampling frequency of 20 MHz. In order to optimize the central frequency of the actuation signal, several actuation signals were generated using central frequencies varying from 10 kHz to 300 kHz in 10 kHz increments. A 4.5-cycle cosine windowed burst signal with a central frequency of 180 kHz was chosen as the actuation signal. Ten observations were recorded at each measurement and the sensor signal was averaged from these observations to reduce the sampling error. Round robin tests were conducted to improve the localization accuracy.

In experiment 1, the composite plate with quasi-isotropic material properties was tested. Baseline data was collected from the healthy composite sample. Guided wave sensor data was collected from the sample with seeded delamination. The Lamb wave signals were analyzed using the MPD algorithm. The Lamb wave modes recorded from both the healthy sample and the sample with seeded delamination were represented in the time-frequency domain. By comparing the two time-frequency representations (TFRs) in the time-frequency domain, the first converted mode caused by the delamination can be identified, as shown in Figure 42. From the TFRs of the master sensor and the nearby slave sensor, the difference of the ToF of the converted mode can be calculated, as shown in Figure 42.

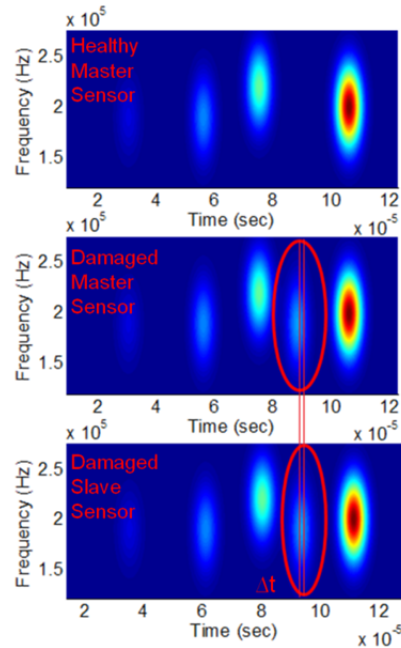


Figure 42. TFRs of the Lamb wave signals collected from master sensor in healthy plate, master and slave sensors from damaged plate

The delamination localization results are shown in Figure 43 a). The real delamination position is 10.2mm away from the estimated delamination position, but still in the 95% confidence range of the estimated delamination area. Experiment 2 validated the developed methodology using the composite plates with orthotropic material properties. Both plain weave and unidirectional fiber fabrics were used. The ToF difference between PZT sensors were computed using the MPD algorithm. The delamination localization results show that the real delamination is 12.6 mm off the estimated delamination position, as shown in Figure 43 b). Experiment 3 validated the developed methodology using the composite plates with two stiffeners. Similar to the approach used previously, the MPD algorithm was used to calculate the ToF difference between sensors. The delamination location was calculated by solving the optimization objective function. Localization results show that the real delamination position is 12.2 mm away from the estimated position, as shown in Figure 43 c). The detailed real and estimated delamination positions in the three examples are shown in Table 10.

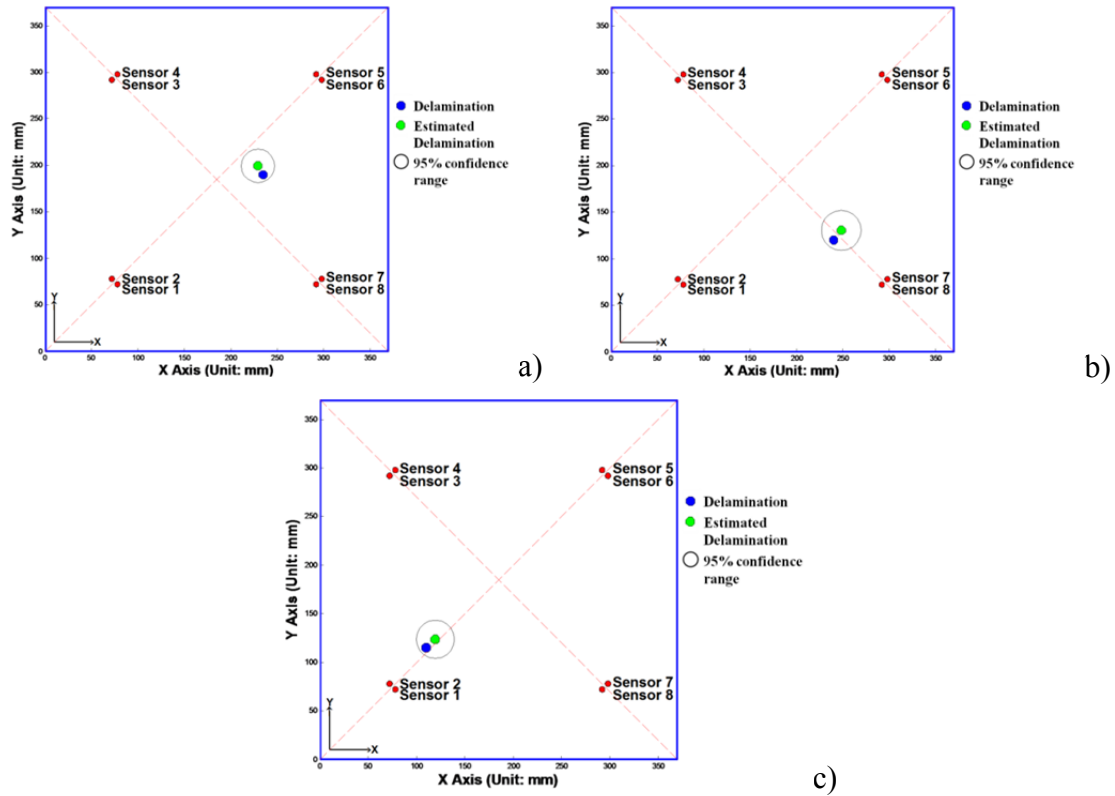


Figure 43. Estimated delamination position and confidence range: a) quasi-isotropic composite panels; b) orthotropic composite panels; c) composite panels with two stiffeners.

Table 10. The real and estimated delamination positions

	Real Position (unit: mm)	Estimated Position (unit: mm)	95% confidence range (unit: mm)
Experiment 1	(235.4,190.7)	(229.3, 199.5)	18.3
Experiment 2	(240.1,120.9)	(248.3, 130.5)	21.5
Experiment 3	(110.2, 115.6)	(119.3, 123.7)	19.8

5.3 Conclusions

An integrated Structural Health Monitoring (SHM) system for damage diagnosis using guided wave mode conversion and time-frequency analysis based MPD algorithm is developed in this project. By using a small time-frequency atom dictionary, the computation cost is reduced significantly. The propagation of Lamb waves in stiffened carbon fiber polymer matrix composite panels is characterized. Each Lamb wave mode is accurately identified using the MPD algorithm. A two-step strategy for detection and characterization of delaminations in stiffened composite panels is developed using the

DISTRIBUTION STATEMENT: Approved for Public Release; Distribution is Unlimited

proposed MPD algorithm. By identifying the converted mode caused by delaminations, the pulse-echo scheme rapidly detects the existence of delamination in the composite panel using only one PZT ring. The pitch-catch scheme detects and quantifies the delaminations in the area between the PZT actuator and sensors. A damage index based on the Lamb wave energy is proposed to quantify the delaminations in composite panels. Multiple damages in one composite sample can be detected.

A delamination localization methodology is further developed using the MPD algorithm. Three pairs of PZTs are used to estimate the damage position. Every two PZTs are placed next to each other. One PZT sensor is used as the master sensor and the others are used as slave sensors. The group velocities of two nearby PZT sensors are assumed to be the same. The difference of ToF between the master and slave sensors is calculated using the MPD algorithm. By solving an optimization function comprising three nonlinear objective equations, the delamination position can be estimated without knowing the group velocity or ToF for each wave mode. Redundant sensors are placed on the surface of composite samples to estimate the 95% confidence range of the delamination position. The proposed localization methodology is experimentally validated using in-house fabricated composite plates and stiffened panels. The experimental results demonstrated that the real delamination positions can be accurately located in the 95% confidence range of the estimated positions.

6.0 PROJECT CONCLUSIONS

This research grant was initiated to investigate SHM techniques on complex composite specimens. Three tasks were initiated with several efforts looking at 1-D and 2-D specimens. Task 1 involved develop a configuration independent framework for damage interrogation and classification that uses virtual and physical sensors for in-situ interrogation and detection and enables prediction of nucleation and growth of defects by applying a high fidelity efficient model. Damage interrogation was conducted using guided wave approach and required investigation of multiple signals and waveforms. At the end of the task, we had established a robust SHM framework capable of assessing system performance under a broad range of thermal and mechanical loading conditions and applied the techniques to a TRAC boom provided by the program manager.

Task 2 was based on investigating advanced information management methods that allow the intelligent use of massive, heterogeneous data from multiple sources. This was not a primary focus based on developments in task 1, but brief efforts were invested into develop techniques that allow efficient analysis of sensor data for SHM and how to exploit intelligent data selection and reduction of massive data from multiple sources. After we identified pertinent data sources for effective integration and relevant features for efficient health monitoring, we examined heterogeneous data sources, data types, and their relationships for feature extraction and damage classification. Time and Frequency techniques were used and developed damage indexes were applied to a 1-D relevant specimen.

Task 3 was used to apply the efforts developed under tasks 1 and 2 to realistic sample with complex features and analyze the developed approaches through demonstrating ability to characterize damage in the structure. Results showed that not only can damage be localized in complex composites using the methods discussed in this report but the challenges associated with anisotropic structures can also be effectively mitigated with proper sensor configuration. Methods developed under this effort can be utilized by any composite platform for ground, air, or space applications.

REFERENCES

- [1] Farrar, C.R., and Lieven, N.A.J., "Damage Prognosis: the Future of Structural Health Monitoring," *Philosophical Transactions of the Royal Society A*, Vol. 365, pp. 623–632, 2007.
- [2] Mohanty, S., Chattopadhyay, A., and Peralta, P., "Adaptive Residual Useful Life Estimation of a Structural Hotspot," *Journal of Intelligent Material Systems and Structures, (special issues on SHM)*, Vol. 21, pp. 321-335, 2010.
- [3] Liu, Y., Mohanty, S., Chattopadhyay, A., "Condition Based Structural Health Monitoring and Prognosis of Composite Structures under Uniaxial and Biaxial Loading," *Journal of Nondestructive Evaluation*, Vol. 29, No. 3, pp: 181-188, 2010.
- [4] Raghavan, A., Cesnik, C.E.S., "Review of Guided-Wave Structural Health Monitoring," *Shock and Vibration Digest*, Vol. 39, pp. 91-114, 2007.
- [5] Zhao, X., Gao, H., Zhang, G., Ayhan, B., Yan, F., Kwan, C., Rose, J., "Active Health Monitoring of an Aircraft Wing with Embedded Piezoelectric Sensor/Actuator Network: I. Defect Detection, Localization and Growth Monitoring," *Smart Materials and Structures*, Vol. 16, pp. 1208–1217, 2007.
- [6] Kessler, S.S., Spearing, S.M., and Soutis, C., "Damage Detection in Composite Materials Using Lamb Wave Methods," *Smart Materials and Structures*, Vol. 11, pp. 269–278, 2002.
- [7] Su, Z.Q., Ye, L., and Lu, Y., "Guided Lamb Waves for Identification of Damage in Composite Structures: A Review," *Journal of Sound and Vibration*, Vol. 295, pp. 753-780, 2006.
- [8] Sohn, H., Park, H., Law, K.H., and Farrar C., "Instantaneous Online Monitoring of Unmanned Aerial Vehicles without Baseline Signals," *In Proceedings of 23rd International Modal Analysis Conference*, Orlando, FN, 2005.
- [9] Giurgiutiu, V., "Tuned Lamb Wave Excitation and Detection with Piezoelectric Wafer Active Sensors for Structural Health Monitoring," *Journal of Intelligent Material Systems and Structures*, Vol. 16, pp. 291-305, 2005.
- [10] Liu, Y., Yekani Fard, M., Chattopadhyay, A., Doyle, D., "Damage Assessment of CFRP Composites Using Time-Frequency Approach," *Journal of Intelligent Material Systems and Structures*, 2012, In Press. (doi: 10.1177/1045389X11433497).
- [11] Fasel, T.R., Todd, M.D., "Chaotic Insonification for Health Monitoring of an Adhesively Bonded Composite Stiffened Panel," *Mechanical Systems and Signal Processing*, Vol. 24, pp. 1420-1430, 2010.
- [12] Lu, Y., Ye, L., Wang, D., Zhong, Z., "Time-Domain Analyses and Correlations of Lamb Wave Signals for Damage Detection in a Composite Panel of Multiple Stiffeners," *Journal of Composite Materials*, Vol. 43, pp. 3211-3230, 2009.
- [13] Banerjee, S., Ricci, F., Monaco, E., Lecce, L., Mal, A., "Autonomous Impact Damage Monitoring in a Stiffened Composite Panel," *Journal of Intelligent Material Systems and Structures*, Vol. 18, pp. 623-633, 2007.
- [14] Staszewski, W.J., Mahzan, S., Traynor, R., "Health Monitoring of Aerospace Composite Structures – Active and Passive Approach," *Composite Science and Technology*, Vol. 69, pp. 1678-1685, 2009.

- [15] Meo, M., Zumpano G., Pigott, M., and Marengo, G., "Impact identification on a sandwich plate from wave propagation responses," *Composite Structures*, Vol. 71, pp. 302-306, 2005.
- [16] Hiche, C., Coelho, C., and Chattopadhyay, A., "A Strain Amplitude-Based Algorithm for Impact Localization on Composite Laminates," *Journal of Intelligent Material Systems and Structures*, Vol. 22, No. 17, pp. 2061-2067, 2011.
- [17] Coverley, P.T., Staszewski, W.J., "Impact Damage Location in Composite Structures Using Optimized Sensor Triangulation Procedure," *Smart Materials and Structures*, Vol. 12, pp. 795-803, 2003.
- [18] Reynolds, W.D., Coelho, C., Kim, S.B., Chattopadhyay, A., Arnold, S.M., "Active Damage Localization in Anisotropic Materials Using Guided Waves," *50th AIAA/ASME/ASCE/AHS/ASC Structures, Structural Dynamics, and Materials Conference (SDM)*, May 4-7, Palm Springs, CA, USA, 2009.
- [19] Moll, J., Schulte, R.T., Hartmann, B., Fritzen, C-P, and O Nelles, "Multi-Site Damage Localization in Anisotropic Plate-Like Structures Using an Active Guided Wave Structural Health Monitoring System," *Smart Materials and Structures*, Vol. 19, pp. 04502-04517, 2010.
- [20] Wang, L., and Yuan, F.G., "Active Damage Localization Technique Based on Energy Propagation of Lamb Waves," *Smart Structures and Systems*, Vol. 3, pp. 201-217, 2006.
- [21] Salamone, S., Bartoli, I., Rhymer, J., Lanza di Scalea, F., and Kim, H., "Validation of the Piezoelectric Rosette Technique for Locating Impacts in Complex Aerospace Panels," *Proceeding of SPIE, Smart Structures and Materials/NDE*, March 6-10, San Diego, CA, USA, 2011.
- [22] Staszewski, W.J., Mahzan, S., Traynor, R., "Health Monitoring of Aerospace Composite Structures – Active and Passive Approach," *Composite Science and Technology*, Vol. 69, pp. 1678-1685, 2009.
- [23] Adewuyi, A.P., Wu, Z. S., "Modal Macro-Strain Flexibility Methods for Damage Localization in Flexural Structures Using Long-Gage FBG Sensors," *Structural Control Health Monitoring*, Vol. 18, pp. 341-360, 2010.
- [24] Mallat, S., Zhang, Z., "Matching Pursuits with Time-Frequency Dictionaries," *IEEE Transactions on Signal Processing*, Vol. 41, pp. 3497-3415, 1993.
- [25] Das, S., Kyriakides, I., Chattopadhyay, A., Papandreou-Suppappola, A., "Monte Carlo Matching Pursuit Decomposition Method for Damage Quantification in Composite Structures," *Journal of Intelligent Material System and Structures*, Vol. 20, pp. 647-658, 2009.
- [26] Chakraborty, D., Kovvali, N., Wei, J., Papandreou-Suppappola, A., Cochran, D., and Chattopadhyay, A., "Damage Classification Structural Health Monitoring in Bolted Structures Using Time-Frequency Techniques," *Journal of Intelligent Material System and Structures*, Vol. 20, pp. 1289-1305, 2009.
- [27] Klein, V., Morelli, E.A., 'Aircraft system identification: theory and practice,' Reston, VA : American Institute of Aeronautics and Astronautics, 2006.

- [28] Juang, J.-N., 'Applied System Identification,' Prentice-Hall, Upper Saddle River, NJ, 1994.
- [29] Polimeno, U., Meo, M., "Detecting barely visible impact damage detection on aircraft composites structures," *Composite Structures*, Vol. 91, No. 4, pp. 398-402, December 2009.
- [30] Van Den Abeele, K.E.-A., Johnson, P.A., Sutin, A., "Nonlinear elastic wave spectroscopy techniques to discern material damage, Part I: nonlinear wave modulation spectroscopy," *Research in Nondestructive Evaluation*, Vol. 12, No. 1, pp.17-30, September, 2000.
- [31] Van Den Abeele, K.E.-A., Carmeliet, J., Ten Cate, J.A., Johnson, P.A., "Nonlinear elastic wave spectroscopy techniques to discern material damage, Part II: single mode nonlinear resonance acoustic spectroscopy," *Research in Nondestructive Evaluation*, Vol. 12, No. 1, pp.31-42, September, 2000.

APPENDIX - Publications and Presentations

1. Liu, Y., Kim, S.B., Chattopadhyay, A., Doyle, D., "Application of System Identification Techniques to Health Monitoring of On-Orbit Satellite Boom Structures," *Journal of Spacecraft and Rockets*, Vol.48, No.4, pp. 589-598, 2011.
2. Liu, Y., Yekani Fard, M., Chattopadhyay, A., Doyle, D., 2012, "Damage Assessment of CFRP Composites Using Time-Frequency Approach," *Journal of Intelligent Material Systems and Structures*, In Press (doi: 10.1177/1045389X11433497).
3. Liu, Y., Kim, S. B., Chattopadhyay, A., Doyle, D., "Damage localization in complex composite panels using guided wave based structural health monitoring system," *Proceedings of the ASME 2011 Conference on Smart Materials, Adaptive Structures and Intelligent Systems (SMASIS)*, September 18-21, Phoenix, AZ, USA, 2011.
4. Vizzini, A.J., Liu, Y., Chattopadhyay, A., "Damage Localization in a Stiffened Composite Panel Using Lamb Wave Based Tomography Approach," *Proceedings of the ASME 2011 Conference on Smart Materials, Adaptive Structures and Intelligent Systems (SMASIS)*, September 18-21, Phoenix, AZ, USA, 2011.
5. Liu, Y., Yekani Fard, M., Kim, S.B., Chattopadhyay, A., Doyle, D., "Structural Health Monitoring and Damage Detection in Composite Panels with Multiple Stiffeners," *52 AIAA/ASME/ASCE/AHS/ASC, Structures, Structural Dynamics, and Materials Conference (SDM)*, April 4-7, Denver, CO, USA, 2011.
6. Liu, Y., Yekani Fard, M., Kim, S.B., Chattopadhyay, A., Doyle, D., "Damage Detection in Composite Structures Using Lamb Wave Analysis and Time-Frequency Approach," *Proceeding of SPIE, Smart Structures and Materials/NDE, March 6-10*, San Diego, CA, USA, 2011.
7. Liu, Y., Kim, S.B., Chattopadhyay, A., Doyle, D., "Structural Health Monitoring of Boom Architectures for On-Orbit Satellites Using System Identification Techniques," *51 AIAA/ASME/ASCE/AHS/ASC, Structures, Structural Dynamics, and Materials Conference (SDM)*, April 12-15, Orlando, FL, USA, 2010.
8. Kim, S.B., Liu, Y., Liu, K.C., Chattopadhyay, A., Doyle, D., "An Integrated Effort for the SHM of On-Orbit Satellites Boom Structures Using Modal Testing and Guided Wave Based Techniques," *51 AIAA/ASME/ASCE/AHS/ASC, Structures, Structural Dynamics, and Materials Conference (SDM)*, April 12-15, Orlando, FL, USA, 2010.

DISTRIBUTION LIST

DTIC/OCP 8725 John J. Kingman Rd, Suite 0944 Ft Belvoir, VA 22060-6218	1 cy
AFRL/RVIL Kirtland AFB, NM 87117-5776	2 cys
Official Record Copy AFRL/RVSV/Derek Doyle	1 cy

(This page intentionally left blank)